Exploring implications of input parameter uncertainties on GLOF modelling results using the modelling code r.avaflow

Sonam Rinzin[1], Stuart Dunning[1], Rachel Joanne Carr[1], Ashim Sattar[2], Martin Mergili[3]

[1]School of Geography, Politics and Sociology, Newcastle University, United Kingdom

[2]Indian Institute of Technology Bhubaneswar

[3]Department of Geography and Regional Science, University of Graz, Austria

Correspondence to: Sonam Rinzin at s.rinzin2@newcastle.ac.uk

Abstract

Modelling complex mass flow processes, such as glacial lake outburst floods (GLOFs), for hazard and risk assessments requires extensive data and computational resources. Researchers often rely on low-resolution, open-access datasets and parameters derived from plausibility due to the difficulty involved in conducting direct measurements. This results in considerable uncertainties in forward modelling, potentially limiting the accuracy and reliability of predictions. To determine the sensitivity of the model outputs stemming from input parameter uncertainties in the forward modelling, we selected nine parameters relevant to GLOF modelling and performed a total of 84 simulations each representing a unique GLOF scenario in the physically-based r.avaflow model. Our results indicate that mass movement-triggered moraine-dammed GLOF modelling outputs are notably sensitive to five parameters, which are, in order of importance: 1) volume of mass movements entering lakes; 2) DEM datasets; 3) the origin of mass movements; 4) entrainment coefficient; and 5) basal frictional angle. The GLOF output parameter resulting from the volume of mass movement impacting lakes has the greatest coefficient of variation (CV) = 47%, while the internal friction angle had the least CV (0.4%). We recommend that future GLOF modelling should carefully consider the output uncertainty stemming from the sensitive input parameters identified here, some of which cannot be constrained before a GLOF and must be addressed using statistical approaches.

1 Introduction

Glacial lakes can store millions of cubic meters of (Zhang et al., 2024; Zhang et al., 2023a; Shugar et al., 2020): as of 2020, it is estimated that glacial lakes (0.002 km^2) store about 1280.6 ± 354.1 km^3 of water in the world (Zhang et al., 2024). The glacial lakes in High Mountain Asia (HMA) have experienced the greatest expansion (46%) between 1990 and 2018 (Shugar et al., 2020). Furthermore, over 28% of glacial lakes in HMA are dammed by loose/destabilizing moraines (Fujita et al., 2013; Zheng et al., 2021b) and the majority of glacial lakes (70%) are exposed to mass inputs in the form of ice/snow avalanches, rockfalls and landslides from the surrounding slopes (Dubey et al., 2023). Meltwater resulting from the shrinkage of glaciers leads to the formation of new glacial lakes and the expansion of existing ones (Zhang et al., 2015; Wang et al., 2020). This process sometimes exposes them to mass movement from the slopes above and increases the total volume of stored water (Rounce et al., 2016). Additionally, the degradation of permafrost destabilizes the slopes surrounding the glacial lakes, increasing the likelihood of mass movements into lakes (Huggel, 2009).

Recent work has documented 3151 GLOF events between 850 and 2022 C.E. globally (Lützow et al., 2023) and 682 GLOF events in HMA between 1833 and 2022 (Shrestha et al., 2023). In HMA alone, these GLOF events have resulted in 6907 human deaths, caused damage to more than 2200 buildings, 71 km^2 of agricultural land, 163 MW capacity of hydropower, 2000 livestock and numerous other structures, including bridges and roads (Shrestha et al., 2023). However, these reported deaths and damages are significantly underestimated because of patchy documentation (Carrivick and Tweed, 2016). The risk from GLOF is expected to rise in the future with the anticipated expansion of glacial lakes (Zheng et al., 2021b; Zhang et al., 2023b) compounded by a growing population and the construction of structures in areas prone to GLOFs (Taylor et al., 2023; Nie et al., 2023).

Most GLOF events in HMA start with mass movements entering the lake from surrounding slopes, leading to the displacement of water and waves overtopping the dam (Shrestha et al., 2023; Lützow et al., 2023; Nie et al., 2018). Mass movements such as rock- or ice-avalanches and landslides entering the lake constitute 70% of known causes of HMA historical GLOF events (Shrestha et al., 2023). The overtopping waves cause moraine dam incision and dam failure, resulting in a sudden discharge of lake water. To a lesser extent, GLOF events are also triggered by factors such as excess hydrostatic pressure from runoff snow and ice melt, intense rainfall and cloud outbursts, and dam settling caused by the melting of ice cores or internal piping. However, it is important to note that in some cases, these triggering factors may not necessarily result in a complete moraine dam failure. As the flood propagates further downstream, it can transform into a debris flow and/ or a hyper-concentrated flow depending

62 on the geologic and topographic characteristics of the river channel as well as depending on
63 the availability of erodible sediment and its grain size distribution (Gaphaz, 2017; Schneider
64 et al., 2014; Westoby et al., 2015; Westoby et al., 2014). These complex GLOF process chains
65 are difficult to accurately capture in numerical models, given the large number of processes
66 and parameters, which limits our ability to model the impacts of the hazard cascade as a
67 whole.

1.1 Numerical modelling of GLOFs

69 Previous studies have used various modelling codes such as HEC-RAS (Sattar et al., 2021b),
70 BASEMENT (Worni et al., 2013; Worni et al., 2012; Byers et al., 2018), FLO-2D (Somos-
71 Valenzuela et al., 2015), RAMMS (Lala et al., 2018), and r.avaflow (Mergili et al., 2020b). Most
72 of these codes, however, cannot model the evolution of the GLOF process chain through
73 interaction at the boundary of different processes involved (e.g. the interaction of mass
74 movements with the lake) and dynamic transformation of flow through sediment entrainment
75 and deposition. To address this limitation, some of the studies modelled each component
76 separately and then fed the results of each modelling component into the next stage (Lala et
77 al., 2018; Schneider et al., 2014; Frey et al., 2018). For example, Lala et al (2018) have used
78 RAMMS to model mass movement from the surrounding slope into the Imja Lake, Nepal,
79 Heller–Hager and BASEMENT to model wave propagation across the lake surface and
80 BASEMENT to model the subsequent downstream hydrodynamic evolution of GLOF. In
81 contrast, the r.avaflow model (Mergili et al., 2017; Mergili and Pudasaini, 2024) enables the
82 integration of all components of the GLOF process chain and their interactions and
83 transformation without the need to combine the results of different models. It enables the
84 detailed modelling of the GLOF process chain, covering everything from the initial trigger to
85 the downstream propagation. r.avaflow is an open-source, GIS-based tool for simulating mass
86 flows over arbitrary terrain. Furthermore, r.avaflow allows modification of all input parameters,
87 which sets it apart from many modelling codes (where most of the parameters remain hidden
88 within a 'black box'), making it suitable for conducting GLOF parameter sensitivity analysis
89 (Mergili et al., 2017; Mergili and Pudasaini, 2024).

90 r.avaflow utilizes the total variation diminishing non-oscillatory central differencing (NOC-TVD)
91 numerical scheme (Wang et al., 2004) to solve an enhanced version of the Pudasaini multi-
92 phase flow model (Pudasaini and Mergili, 2019). It also offers added features for entrainment,
93 deposition, dispersion, and phase transformation. Because of these features, r.avaflow can
94 model the full process chain of a GLOF and flow transformation due to erosion of bed material
95 and deposition of entrained material (Mergili et al., 2017; Mergili and Pudasaini, 2024).
96 However, the precision of this model output parameters such as peak flow, depth and velocity

depends on the accuracy of various input parameters and initial conditions, including the release height of mass, the resolution and vertical accuracy of the digital elevation model (DEM), density, entrainment, and frictional parameters (Mergili et al., 2017).

Because of the significant logistic challenges associated with collecting field data and the financial costs involved in acquiring high-resolution remote sensing data, many of the parameters in GLOF modelling are derived from open-access data, leading to considerable uncertainties in the resultant discharge, inundation extent, and arrival times. Also, certain input parameters such as the volume of mass movement entering the lake are impossible to measure accurately before a GLOF event. For example, the global-scale DEM, SRTMGL1, with a ground resolution of 30 m, is commonly employed in GLOF modelling without adequately considering the inherent uncertainty due to horizontal and vertical inaccuracies in this DEM (Rinzin et al., 2023). Similarly, the origin of avalanches and other mass movements is determined using low to medium-resolution remote sensing imagery and DEM, often supplemented by secondary datasets like permafrost data (Obu et al., 2019), which can introduce notable uncertainties (Sattar et al., 2023; Allen et al., 2016). When estimating the volume of avalanches entering lakes, DEM differencing between pre- and post-event conditions can be advantageous for reconstructing historical events (Baggio et al., 2021; Zheng et al., 2021a), although the accuracy is contingent upon the vertical and horizontal accuracy and resolution of the data, and the temporal interval between data acquisition. Likewise, when ice is considered the sole source of the mass movement, ice thickness is employed to calculate the avalanche volume (Allen et al., 2022), for which the accuracy of computed volume relies on the resolution and availability of ice thickness data from the ice-flow inversion model in the region of interest. Under circumstances when the depths of landslides and avalanches are not known, arbitrary thicknesses of 10, 30, and 50 m based on past events (Dubey et al., 2023) are often utilised for forward modelling, further contributing to significant uncertainties in the modelling results (Rounce et al., 2017; Rounce et al., 2016; Dubey and Goyal, 2020).

Moreover, the flow parameters in r.avaflow are adjusted and optimised based on the fit of the model's results to well-documented past events (Mergili et al., 2017; Mergili et al., 2020a; Vilca et al., 2021) and the physically plausible range suggested by Mergili et al. (2017), Mergili et al. (2018b) and Mergili et al. (2018a). Efforts to fine-tune parameters to fit with historical events of varying magnitude, temporality and spatiality have led to the use of wide-ranging values. For example, Mergili et al. (2020b) used an internal solid friction angle of 28° to reconstruct the 1941 GLOF process chain of Lake Palcacocha in the Cordillera Blanka, Peru. In contrast, Vilca et al. (2021) used 45° to model the 2020 glacial lake outburst process chain of Lake

132   Salkantycocha located in Cordillera Vilcabamba of Peru. Likewise, the value of the basal
133   friction angle ranges between 6-18° (Baggio et al., 2021; Mergili et al., 2020a) (Supplementary
134   Figure 1 (Fig. S1)). Because each GLOF event is inherently distinct, even when originating
135   from the same glacial lake (Emmer and Cochachine, 2013; Lala et al., 2018), inferring
136   reconstructed values from past events for forward modelling introduces substantial
137   uncertainties (Gaphaz, 2017; Mergili et al., 2020b). Finally, r.avaflow model outputs are
138   extremely sensitive to parameters like entrainment coefficient value, basal friction angle and
139   initial release volume (Mergili et al., 2018b; Mergili et al., 2018a; Baggio et al., 2021). While
140   all these indicate that the value of input parameters is highly variable depending on specific
141   events, to our knowledge, how changes in the values of these input parameters affect the
142   model output (for example, peak and total flow, flow depth, flow velocity and arrival time) is
143   not known.

144   To determine the relative contribution of uncertainties in different input parameters to variability
145   in GLOF extent, we identified nine out of 38 input parameters and initial conditions relevant to
146   GLOF flow modelling: digital elevation model; the volume of mass movement impacting the
147   lake; the origin of mass movement impacting the lake; grain density of mass movement
148   impacting the lake; volume of lake; entrainment coefficient; internal friction angle; basal friction
149   angle; and, fluid friction number (Table S1). Our selection was motivated by the recognition
150   that these input parameters are considered essential and have been frequently adjusted in
151   previous studies to align with values inferred from observed past (Baggio et al., 2021; Mergili
152   et al., 2018b; Allen et al., 2022; Zheng et al., 2021a; Vilca et al., 2021). We believe that these
153   parameters are the most likely to influence the results of future modelling efforts, making it
154   critical to evaluate their impacts on model outputs. We assessed the sensitivity of the model
155   output to each of these parameters by conducting up to 10 r.avaflow simulations per parameter
156   and varying their values within the range determined from the literature that employed
157   r.avaflow modelling (Fig. S1). We investigated the impact of variation in these parameter
158   values on the model outputs and used the following diagnostic variables: peak discharge; total
159   discharge; flow arrival time; flow depth; flow velocity and reach distance. We then calculated
160   the coefficient of variation for each parameter and ranked them based on this metric.

161   **2 Study site**

162   Here, our sensitivity analysis was conducted on Thorthormi Tsho located at 28.10° N, 90.27°
163   E in the Lunana region of the Bhutan Himalaya (Fig. 1). The area of Thorthormi Tsho has
164   expanded by ~192% since 1990, evolving into the largest proglacial lake (area = 4.35 km^2) in
165   Bhutan by 2020 (Rinzin et al., 2023) (Fig. 1B and 1E). Although the lake level was lowered by
166   5m by artificially draining out the water between 2008 and 2012 (Nchm, 2019a), Thorthormi

Tsho is marked as the most dangerous glacial lake as it is determined to be susceptible to triggering factors (like mass movement entering lake) and potentially unstable moraine damming the lake (Nchm, 2019a; Rinzin et al., 2021) (Fig. 1B). In recent years, Thorthormi Tsho has produced two GLOF events (Nchm, 2023); the first one occurred on June 20, 2019 (Nchm, 2019b), the latest on October 30, 2023. Also, modelling of future predicted GLOF from Thorthormi Tsho shows it can produce a flood with flow volume up to 3×10^8 m^3 of water with a peak discharge of up to 75000 m^3 s^{-1}, affecting more than 16000 people and various infrastructures downstream of this glacial lake (Rinzin et al., 2023). This high outburst susceptibility and hazard make Thorthormi Tsho an ideal candidate for GLOF modelling to improve our modelling output GLOF uncertainty.
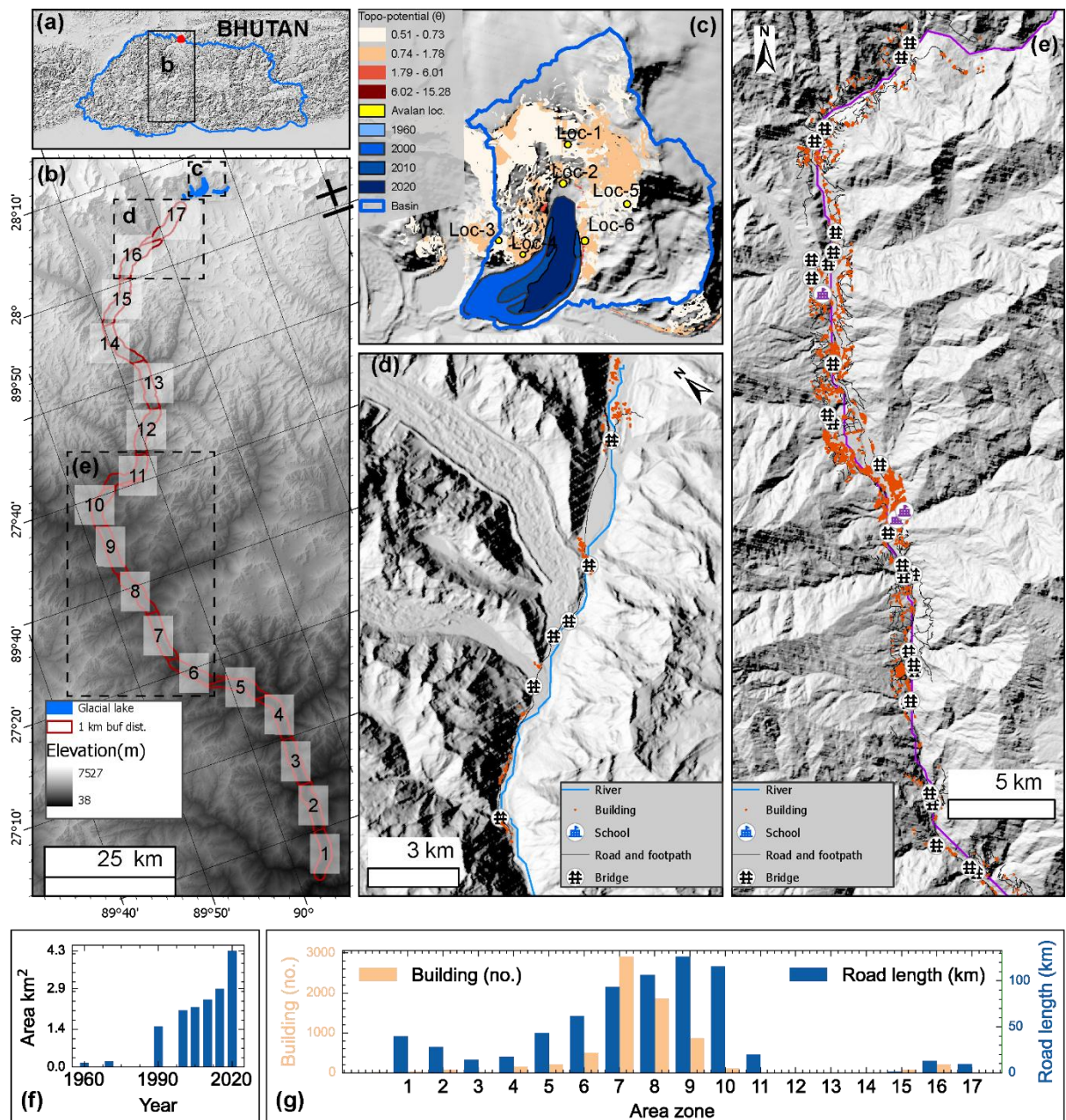
Figure 1: Study area. The map (a) indicates the location of Thorthormi Tsho and its downstream condition in Bhutan. The map (b) shows elevation and the overview of glacial lakes in Lunana and settlements along the Phochu and Punatsangchu basins, downstream of Thorthormi Tsho. The downstream settlement is divided into 17 zones (1-17), each 10 km long. (c) Area of Thorthormi Tsho between 1960 and 2020, and the surrounding slope with topography potential (TPP) for mass movement entering Thorthormi Tsho. he downstream settlements in the (d) Lunana and (e) Punakha and Wangdue Phodrang regions. The bar graphs are (f) the change in the area of Thorthormi Tsho between 1960 and 2020 (Rinzin et al., 2023) and (g) the buildings (count) and road (km) within the 1 km on either side of the river centreline as per the latest OpenStreetMap (as of 30th Mach 2024). Loc-1 to Loc-6 are the locations of origin of mass movement entering the lake considered for this study.

Additionally, the Phochu and Punatsangchu basins, located downstream of Thorthormi Tsho, are the most populated basins in Bhutan. The latest updated (as of 30th March 2024) OpenStreetMap (https://www.openstreetmap.org) although it does not have 100% coverage, shows that there are over 7000 buildings, 50 bridges, 4 schools, 687 km of road and a large area of agricultural land within the 1 km radius of the Phochu and Punatsangchu rivers (Fig. 1c,1d,1f). Besides, located downstream are the two biggest hydropower plants (Punatsangchu-1 and Punatsangchu-2) in Bhutan, poised to become key contributors to the nation's GDP. Also, the Punakha Dzong, which has great historical and cultural significance to Bhutan is located downstream of Thorthormi Tsho. This high downstream exposure to GLOF hazard further highlights the importance of understanding GLOF characteristics from Thorthormi Tsho for GLOF modelling (Fig. 1).

3 Methods

3. 1 r.avaflow model framework

r.avaflow is a comprehensive GIS-based open-source computational framework for modelling mass movement from one or more release areas over the defined basal topography (Mergili et al., 2017; Mergili and Pudasaini, 2024). It can model the entire GLOF process chain starting from the release of avalanches, through the dynamic interaction of the avalanche and lake water, then the overtopping and retrogressive moraine dam erosion, and finally the downstream evolution of the resulting flow (Mergili et al., 2020b; Vilca et al., 2021; Sattar et al., 2023). It can also robustly consider the interactions between the phases as well as erosion and deposition (Mergili et al., 2017). Furthermore, it is equipped with a built-in function for visualization and validation. Because of this capability, r.avaflow has been widely used to model process chains such as GLOF in the high mountains all over the world, mostly to

212   reconstruct past events (Zheng et al., 2021a; Mergili et al., 2020b; Vilca et al., 2021) and to a

213   lesser extent to predict future hazards (Sattar et al., 2023; Allen et al., 2022).

214   In r.avaflow, the evolution of the flow in space and time is solved by using an enhanced version

215   of the Pudasaini multiphase flow model (Pudasaini and Mergili, 2019; Pudasaini, 2012). The

216   flow is computed through depth-averaged conservation of mass and momentum equations for

217   solid and fluid components. These equations involve six differential equations accounting for

218   solid (D_s) and fluid (D_f) flow depths, solid (M_{sx}) and fluid (M_{fx}) momentum in x direction (M_{sx} =

219    $D_s.v_{sx}$, $M_{fx} = D_f.v_{fx}$), and M_{sy} and M_{fy} in y direction ($M_{sy} = Ds.v_{sy}$, $M_{fy} = D_f.v_{fy}$), where v is the

220   flow velocity (Mergili et al., 2017). Mohr-Coulomb plasticity is used to compute solid stress

221   while fluid is subjected to solid volume-fraction-gradient-enhanced non-Newtonian viscous

222   stress. r.avaflow also considers other factors like virtual mass force, viscous drag, and

223   buoyancy. These factors collectively facilitate momentum transfer between the solid and fluid

224   phases, enabling simultaneous deformation, separation, and mixing of phases as they

225   propagate across the mountain topography (Pudasaini and Mergili, 2019; Pudasaini and

226   Krautblatter, 2014b; Mergili et al., 2020b; Pudasaini, 2012). To numerically solve these

227   differential equations and propagate flow over time and space, r.avaflow uses a high-resolution

228   total variation diminishing non-oscillatory central differencing (TVD-NOC) scheme, a

229   commonly used numerical scheme to handle the advection of quantities, whilst minimising

230   numerical artefacts like oscillations (Wang et al., 2004). The internal friction angle and basal

231   friction angle, which are crucial factors governing the frictional forces influencing flow rheology,

232   are adjusted based on the solid fraction of the flow material (Mergili et al., 2018b; Mergili et

233   al., 2017; Pudasaini and Mergili, 2019).

234   r.avaflow has three different models, namely, a single-phase shallow water model with Voellmy

235   friction relation, an enhanced version of the multi-phase-flow of Pudasaini and Mergili (2019)

236   and an equilibrium-of-motion model for slow-flow process (Mergili and Pudasaini, 2024) Here,

237   we chose an enhanced version of the multi-phase-flow model considering an erodible moraine

238   dam and mass movement entering the lake as the solid component and lake water as the fluid

239   component. The multi-phase mass flow model can simulate the propagation of three different

240   elements: solid (coarse material including boulders, cobbles and gravel), fine solid (including

241   sand and particles larger than clay and silt), and fluid (including water and very fine particle

242   including clay, silt and colloids), and assign each of them with distinct flow rheology (Pudasaini

243   and Mergili, 2019).

244   Furthermore, r.avaflow has six specific optional functions including conversion of release

245   height to depth, diffusion control, surface control, entrainment, stopping and dynamic adaption

246   of friction parameters. The latest version of r.avaflow has four options to compute erosion and

entrainment, (i) calculated by multiplying the entrainment coefficient with flow momentum, (ii) simplified entrainment-deposition numerical model of Pudasaini and Krautblatter (2014a); (Mergili and Pudasaini, 2024), (iii) a combination of (i) and (ii), and (iv) acceleration-deceleration entrainment and deposition model. Since models (ii) to (iv) are at the experimental phase, here, we used model (i), where the amount of entrainment is computed dynamically by multiplying with the user-defined entrainment coefficient (CE) with the total momentum of the flow at the given raster cell and time step (Mergili et al., 2017) (equations 1 and 2).

$$q_{E,s} = C_E|M_s+M_f| \, \alpha_{s,Emax} \tag{1}$$

$$q_{E,f} = C_E|M_s+M_f| \, (1- \alpha_{s,Emax}) \tag{2}$$

Where q_{Es} and q_{Ef} are the entrainment rates of solid and fluid respectively

C_E is user user-defined entrainment coefficient (kg^{-1})

$\alpha_{s, Emax}$ is using user-defined solid entertainable material height (m)
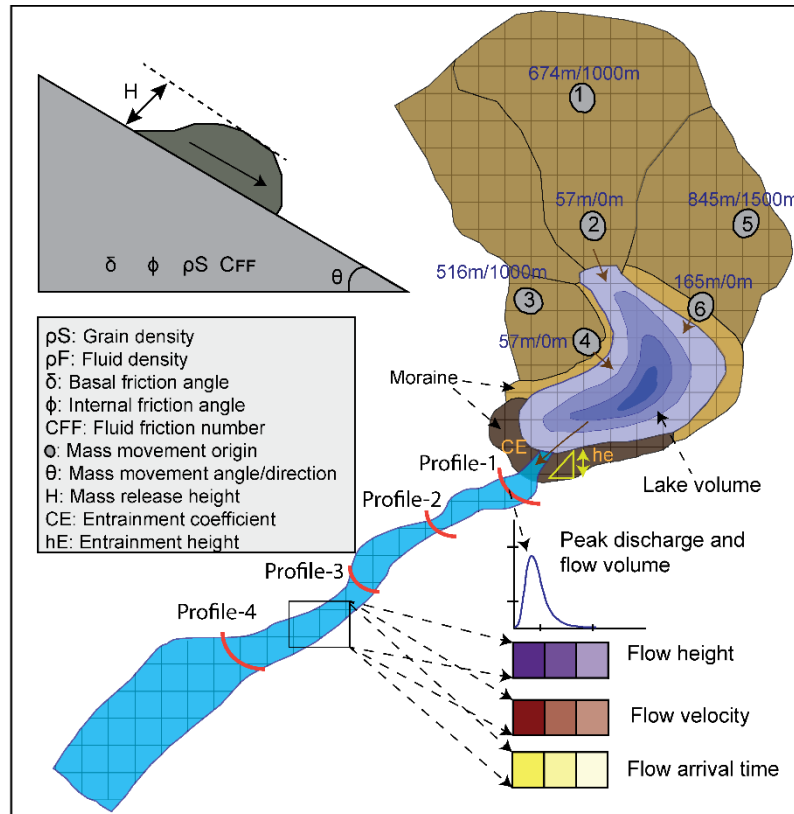
Figure 2: Schematic view of Thorthormi Tsho, surrounding terrain (study area) and input parameters employed for investigating r.avaflow model output sensitivity used in this study. 1-

262   6 shows the origin of the mass movement entering the lake (considered for this study) with
263   vertical drop/horizontal distance to the lake shoreline.

264   We utilized r.avaflow direct, a web-based tool (Mergili and Pudasaini, 2024), to initially
265   generate the sample model script. We modified the sample script by inputting parameters
266   relevant to each experimental set-up and wrote a bash shell script for all simulations in each
267   experiment to test various parameter values within our predefined range. We developed one
268   master bash script for each experiment that allowed us to run all experiments in parallel
269   leveraging the Rocket High Performance Computing (HPC) facilities at Newcastle University.
270   All the GLOF simulations were done for Thorthormi Tsho and were run for 1500 seconds when
271   the flow reaches up to ~24 km downstream of the lake depending on values of various
272   parameters defined here. The flow propagation beyond this point and its interaction with the
273   downstream component are beyond the scope of this study.

274   **Table 1:** Key parameters tested in this study to investigate model output sensitivity. Detailed
275   parameters for r.avaflow modelling are provided in Table S1. The constant value is the
276   common parameter value used across experimental setups.

Parameter	Value range	No. of simulations	Constant value
Topographic data (DEM)	High Mountain Asia DEM (HMA-DEM) (8m), AW3D30 (30m), NASADEM (30m), SRTMGL3 (90 m)	4 (1×4)	HMA-DEM
Origin of mass movement	Left (2), Right (2), Headwall (2)	6	Loc-1
Volume of mass movement	$1 - 10 \times 10^6$ m^3	10	5×10^6 m^3
Grain density of mass movement	1000 – 2700 kg/m^3	10	2700
Lake volume	2 to 3.8×10^8 m^3	10	3×10^8 m^3
Entrainment coefficient	$10^{-5.85} - 10^{-6.95}$ kg^{-1}	10	$10^{-6.35}$
Basal friction angle	$10 - 14^\circ$	10	10
Internal friction angle	$25 - 35^\circ$	10	28
Fluid friction number	0.027 – 0.050	10	0.05

277   **3.2 Model inputs parameterisation and experimental setups**

278   In the context of r.avaflow, a parameter is an (often user-defined) variable influencing the
279   physical characteristics of the movement or the numerical behaviour" of the flow. Parameters

280 can be based, e.g., on physics (such as friction angles) or empirical knowledge. Parameters
281 can be represented by global values, by individual values for each raster cell, or by time-
282 dependent values. r.avaflow has a large choice of parameters and initial conditions, such as
283 a DEM representing initial basal topography, the volume of the solid and liquid phase,
284 entrainment and stopping parameters and density and friction parameters (Mergili and
285 Pudasaini, 2024) (Table S1). The values specified for these parameters influence crucial
286 aspects of modelled GLOF flow characteristics, including impacted area, travel distance, travel
287 time, and volume of sediment deposited at the various downstream locations (Mergili et al.,
288 2017). In this study we selected a total of nine parameters which are identified as important
289 and commonly modified in the previous studies (e.g. Mergili et al. (2020a)): 1) DEM dataset;
290 2) volume of mass movement entering the lake (V_S); 3) the origin of mass movement into the
291 lake; 4) volume of glacial lake (V_L) 5) grain density of mass movement entering the lake (ρS);
292 6) entrainment coefficient (C_E); 7) basal friction angle (δ); 8) internal friction angle (ϕ); 9) fluid
293 frictional number (C_{FF}). To investigate the impact of DEM dataset variation, we modelled GLOF
294 by employing freely available global and regional DEM datasets with differing spatial resolution
295 and vertical accuracy (Table 2). For the origin of the mass movement entering the lake, we
296 first computed the topographic potential for mass movement into the lake (Allen et al., 2019)
297 (Fig. 1B) and selected six different sites by considering the topographic potential values and
298 geometry of the lake (Fig. 2). The V_S was varied between $10^6 - 10^7$ m^3. The ρS value range
299 was considered based on assumed combinations of rock and ice parts in mass movement
300 following the approach used in the earlier studies (Allen et al., 2022; Sattar et al., 2023). For
301 parameters 5-9, we gathered various values employed in previous studies (Allen et al., 2022;
302 Mergili et al., 2020a; Mergili et al., 2020b; Vilca et al., 2021) and computed descriptive statistics
303 and established the median, upper quantile value, and lower quantile for each parameter using
304 these collated values (Fig. S1). We then varied these parameter values between the
305 calculated upper quartile and lower quartile, to give 10 equally spaced values in total. This
306 range of 10 values was utilised in a total of 10 experiments for each respective parameter,
307 whilst holding other parameter values constant at the median value. For example, for the ϕ
308 experiment, the value of ϕ was varied between the upper and lower quantiles, with 10
309 increments in total, whilst holding constant the other parameter values (Table 1). An overview
310 of employed parameters and workflow is shown in Fig. 2 (schematic view) and Table 1, while
311 further details on the parameter range used for each experiment are provided in the following
312 section.

313 **Table 2:** Characteristics of DEM datasets employed in this study to investigate the impact of
314 DEM dataset variation on GLOF modelling results.

DEM dataset	Acquisition techniques	Spatial resolution	Vertical accuracy	Coverage	Survey date
AW3D30	Optical stereo images	~30 m	6.84 m (RMSE relative to ICESat in HMA) (Liu et al., 2019)	Global	2006 to 2011
NASADEM	SAR Interferometry	~30 m	5.3 m (RMSE for USA) (Liu et al., 2019)	Global	2000
SRTMGL3	SAR Interferometry	~90 m	9.51 m (RMSE relative to ICESat in HMA) (Buckley et al., 2020)	Global	2000
HMA-DEM	Optical stereo images	8 m	2-m (depending on the type of sensor) (Shean, 2017a)	High Mountain Asia (HMA)	2002 to 2016

3.2.1 Digital Elevation Model

Here our goal is to constrain model output uncertainty stemming from the use of freely available global and regional DEM datasets. We performed a series of GLOF simulations using four open-access DEM data of various resolutions, vertical accuracy and elevation derivation methods, namely, High Mountain Asia DEM (HMA-DEM; 8 m) (Shean, 2017b), ALOS Global Digital Surface Model (AW3D30; 30 m) (JAXA, 2021), NASADEM (~30 m) (Nasa-Jpl, 2021), and SRTMGL3 (~90 m) ((Srtm), 2013) (Table 2). The details about the DEM datasets used here are provided in the supplementary information.

3.2.2 Volume of glacial lake and mass movement entering the lake

r.avaflow has the option to define the initial release volume of different phases involved in the GLOF process chain. Here, we assume the GLOF was initiated by rock-ice mixed mass movement entering the lake followed by a tsunami wave hitting the moraine damming the lake and causing moraine dam failure. Accordingly, we defined the frontal moraine damming Thorthormi Tsho as phase-1 (rock component with $\rho = 2700$ kg m^{-3}), mass movement entering Thorthormi Tsho as phase-2 (rock-ice component) and Thorthormi Tsho as phase-3 (fluid part).

Field-based bathymetric data is essential for accurately estimating the V_L, which is a fundamental input for the GLOF modelling. However, the remote and harsh environment of glacial lakes in the mountain regions makes it highly challenging to conduct field-based bathymetric surveys. In the case of Thorthormi Tsho, conducting the bathymetric survey is particularly difficult as the lake is filled with debris and icebergs, which makes it hazardous to conduct survey. In the absence of field-based bathymetry, the area-volume empirical equations are commonly employed by past studies to approximate the V_L. However, these area-volume scales are based on sparse field data and may not represent the actual volume, leading to substantial uncertainties in the volume estimates (Zheng et al., 2021a; Gantayat et

al., 2024). In this study, we calculated the volume of Thorthormi Tsho considering eight area volume empirical equations which are commonly used for computing the volume of moraine dam lakes (Table S2). Uncertainty in using these empirical equations where evident as the V_L estimate for Thorthormi Tsho ranges between 2.1×10^8 m³ to 3.8×10^8 m³. So, to investigate the impact of this uncertainty on modelled GLOF hydraulics, we modelled 10 scenarios of GLOF by varying V_L from 2.0×10^8 m³ to 3.8×10^8 m³ with increments of 20×10^6 m³. For all other experiments, the median value (2.9×10^8 m³) of V_L estimated from area-volume scaling equations was used uniformly. r.avaflow requires spatially varying lake bathymetry to be used as fluid release height rather than the absolute V_L. Thorthormi being a recently formed lake, has ice thickness data covering the extent of the lake (Farinotti et al., 2019). Therefore, we computed the bathymetry of Thorthormi Tsho by subtracting ice thickness data from the surface DEM (Linsbauer et al., 2016; Linsbauer et al., 2017). Assuming that the present-day lake has been formed by filling the over-deepening, this ice-thickness-derived bathymetry was adjusted to match the volume we employed for each modelled GLOF. For example, for the experiment with a V_L of 3×10^8 m³, the ice thickness bathymetry was adjusted to get the same volume (Table S2).

The volume of mass movement entering the lake serves as a fundamental parameter for defining various scenarios in the forward modelling of a GLOF (for example, Allen et al. (2022) and Sattar et al. (2023)). However, it is difficult to predict how big or small the mass movement will be. The historical record of V_S is sparse but mostly exceeds 1×10^6 m³ (for example, Zheng et al. (2021a) and Byers et al. (2018)), although a recent event in Sikkim Himalaya was known to have been caused by a volume of up to 14.7×10^6 m³ (Sattar et al., 2025). Additionally, earlier studies in Nepal based on topographic potential and assumed three depths based on avalanches in Russia and the Swiss Alps (10m, 30m and 50 m) (Rounce et al., 2016) has estimated the volume between 2.7×10^6 to 6.7×10^6 m³. Here we selected the most likely zone of mass movement entering lakes based on the topographic potential of the slope surrounding the lake. However, accurately constraining the V_S remains highly challenging and subject to considerable uncertainty. Considering these uncertainties, to test the effect of mass movement of various volumes, we conducted a series of 10 experiments considering V_S ranging from 1×10^6 to 10×10^6 m³. For the other experiments, we used a uniform V_S of 5×10^6 m³ (Table 1).

3.2.3 Origin of mass movement into the lake

To account for uncertainties involved in the origin of mass movement entering the lake, we identified a total of six mass movement areas, each characterised by different directions and distances to the lake (Fig. 1 and Fig. 2). To do this, we first computed topographic potential for

374 mass movement (ice/rock avalanche and landslide) into the lake based on slope and run-out

375 trajectory criteria (Allen et al., 2019). Based on this first-order estimate, we identified the six

376 potential mass movement origin each with unique direction, height, and distance relative to

377 the lake (Fig 2): Loc-1 (slope at ~1 km away from the headwall, aligned along the longitudinal

378 axis), Loc-2 (headwall about 100 m away from the lake along the longitudinal axis), Loc-3

379 (slope at the 1 km from right moraine dam), Loc-4 (right moraine dam), Loc-5 (slope at ~1.5

380 km from left moraine dam), Loc-6 (left moraine dam) (Fig. 1 and Fig. 2). We then ran one

381 scenario of GLOF from each of these locations (total = 6) keeping all input variables constant

382 for each model run. For the rest of the experiments, we used a mass movement scenario from

383 loc-1.

384 **3.2.4 Grain density of mass movement entering the lake**

385 Our goal here is to assess the impact of ρS entering the lake, which serves as a proxy for the

386 ice-to-rock ratio. Accordingly, we consistently set the grain density of phase-1 (moraine) at

387 2700 kg m^{-3} across all the experiments, whilst the fluid density of phase-3 was also held

388 constant at 1000 kg m^{-3}. In the earlier studies, ρS has been used as a proxy of the portion of

389 an ice-rock component of mass movement into the lake, which is highly uncertain (Vilca et al.,

390 2021; Allen et al., 2022). The phase separation of rock and ice components of the mass

391 movement with different densities is not well established in r.avaflow (Vilca et al., 2021).

392 Therefore, in this study, following Sattar et al. (2023), a portion of snow and ice in the mass

393 movement is considered fluid by adjusting the ρS of the phase-2 represented by the mass

394 (Table S3). In our experiment set-up, this is executed by varying the ρS value between 2700

395 kg m^{-3} (representing 100% rock) to 1000 kg m^{-3} (representing 100% ice) (Table 1).

396 **3.2.5 Entrainment coefficient**

397 Material entrainment due to bed erosion can make the flow more concentrated and thus

398 increase the volume, resulting in spatial and temporal variation of flow. In the r.avaflow model,

399 the user must define entrainment height in the form of a raster covering the entire model

400 domain, which can be either identified using remote sensing imagery or fieldwork (Mergili and

401 Pudasaini, 2024). However, accurately measuring the depth and spatial extent of these

402 erodible materials covering the entire model domain is highly challenging, even with field

403 surveys, and remains infeasible using remote sensing techniques alone. In this study, we

404 focused on the frontal moraine, as it is measurable using remote sensing data. The extent of

405 the moraine was mapped using high-resolution Google Earth imagery, while its height was

406 determined using the HMA-DEM (Fig. 1). The amount of entrainment itself is dependent on

407 the user-defined C_E. In r.avaflow the logarithm with base 10 of the C_E must be entered (Mergili

408   et al., 2018a; Mergili et al., 2017). Here, we modelled 10 scenarios of GLOF by varying C_E

409   between $10^{-6.95}$ to $10^{-5.85}$ kg^{-1} (Table 1).

410   **3.2.6 Frictional parameters**

411   The internal friction angle (ϕ), basal friction angle (δ) and fluid friction number (C_{FF})

412   mechanically control the basal shear stress, internal deformation, anisotropy of the stresses,

413   and hydraulic pressure gradient of the solid constituents (Pudasaini and Krautblatter, 2014b),

414   which are essential attributes influencing flow runout distance and time. Within the r.avaflow

415   model set-up, a user can either use spatially varying values for these frictional parameters

416   using a raster map or one absolute value (Mergili and Pudasaini, 2024; Mergili et al., 2017).

417   In this study, we computed 10 experiments for each of these frictional parameters. Specifically,

418   by varying ϕ between 25° to 35°, δ between 10° and 14° and C_{FF} between 0.027 to 0.050 (Table

419   1).

420   **3.3 Sensitivity Analysis**

421   Here we use sensitivity analysis, to determine how variations in the initial values for key input

422   parameters impact the modelled GLOF hydraulics (Saltelli et al., 2004). Thus, our goal is not

423   to determine the 'correct' value for each parameter but to determine the r.avaflow input

424   parameter(s) that cause the most variation in the model output. To constrain this variability, we

425   mainly focused on examining the peak discharge, total discharge, and flow arrival time as the

426   output metrics. The flow for all the experiments was measured from the profile immediately

427   beneath the moraine dam (profile-1 in Fig. 2). We calculated the peak and total discharge

428   based on the flow data obtained from the same profiles (Fig. S2). The flow arrival time was

429   considered as the average value across the time recorded from the profiles located 3 km, 6

430   km and 9 km downstream of the Thorthormi Tsho (profile-2, 3, 4 in Fig. 2). For the scalable

431   parameters, we also computed simple linear regression considering input parameters as the

432   independent variable and model output as the dependent variable. To ascertain the sensitivity

433   of the three model output metrics defined earlier to variations in value across all parameters,

434   we computed the coefficient of variation (CV) for individual parameters and subsequently

435   ranked them based on this metric. The CV is a statistical measurement of the dispersion of

436   data points around the mean, regardless of the units used to measure it. CV is deemed

437   suitable here since the r.avaflow output variability is caused by input parameters that are

438   measured in different units. To calculate CV, we took the standard deviation of the output value

439   range of a particular experiment (e.g. peak discharge) and divided it by the mean of the same

440   output range (Abdi, 2010). We multiplied each CV value by 100 to express them in percentage

441   form.

4 Results

4.1 Effect of DEM dataset

When the GLOF was modelled employing freely available global and regional DEM datasets (HMA-DEM, AW3D30, NASADEM, SRTMGL3), our results showed a variation of peak and total discharge of GLOF from the Thorthormi Tsho by almost 100% and 400%, respectively (Fig. 3). Specifically, HMA-DEM consistently produced the lowest GLOF magnitude, while SRTMGL3 consistently produced the highest. Although NASADEM and AW3D30 have a similar spatial resolution, notable differences (65%) in peak discharge and other hydraulic properties emerged between simulations done using these datasets (Fig. 3a).

We observed a significant fluctuation in the mean flow depth (82%) and velocity (43%) along the flow path resulting from the change in DEM datasets (Table. 3). For instance, the mean flow depth along the river centreline ranged from 39 m (HMA-DEM) to 54 m (SRTMGL3) (Table 3) and the flow reach distance increased from 15.5 km (HMA-DEM) to 24.2 km (SRTMGL3). Once again, NASADEM and AW3D30 yielded significantly different maximum flow depths (8.5%) and reach distances (72%) (Fig. 3b). The flow arrival time varied by around 59%. Flows derived from SRTM data always arrived earlier, while those using HMA-DEM were consistently most delayed (Fig. 3c). There was also a similar variation in the solid concentration of the flow in response to changes in input DEM datasets (Fig. 3b).
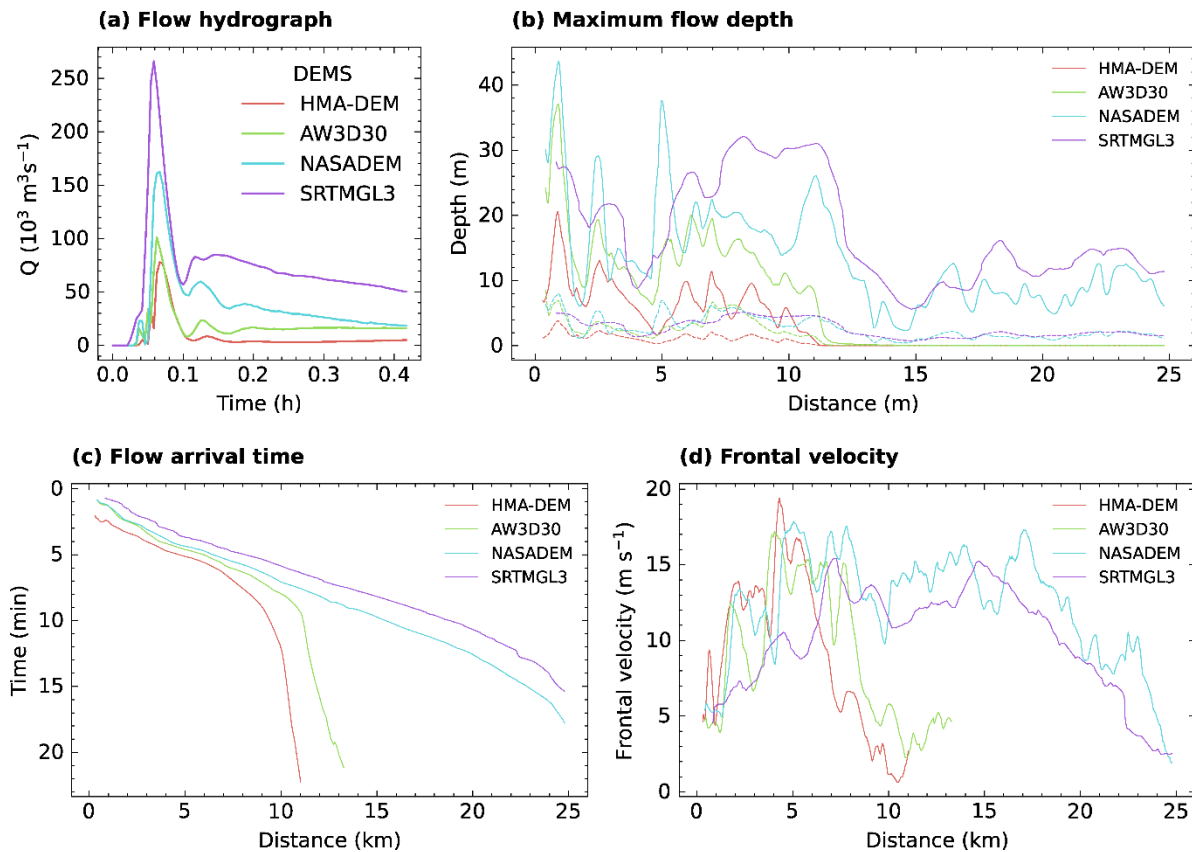
Figure 3: The line graph (a) showing hydrographs, (b) maximum flow depth (for total and debris part), (c) flow arrival time and (d) flow velocity profiles along the river centerline generated by conducting a sequence of r.avaflow simulations, employing different types of DEM datasets. The solid and dashed lines (in panel a) show the maximum flow depth and debris part of the flow. The profiles are plotted as rolling averages every 100 m.

Table 3. Percentage change in flow velocity, depth and arrival time resulting from variation in values of different input parameters we employed in this study. The total percentage (%) change represents the output variation between the maximum and minimum values used in the experiment. The average percentage (%) change is calculated as the mean change across all incremental steps employed in setting up the experiment. The arrival time average of the record from three locations, Profile-2, -3, and -4) (Fig. 2). Flow velocity and depth are mean values taken from the river centreline. The negative (-) value indicates that increasing input parameters decreases output parameters. The detailed flow pattern along the river centreline is provided in Fig. S3, Fig. S4, Fig. S5 and Fig. S6.

No.	Parameter	Velocity (% change)		Depth (% change)		Time (% change)	
		Average	Total	Average	Total	Average	Total
1	DEM dataset	16.25	43	20.5	82	20	59

2	Volume of mass movement entering lake	9.2	92	92.3	923	-14.3	-143
3	Density of mass movement entering the lake	0.2	2	3.1	31	-0.6	-6
4	Origin of mass movement entering the lake	10.8	65	8.2	82	3.3	20
5	Volume of glacial lake	0.1	1	0.1	1	-4	-9
6	Entrainment coefficient	-1	-10	-4.9	49	3	3
7	Basal friction angle	-2.3	-23	-4.2	42	6.8	68
8	Internal friction angle	-0.1	-1	-3.8	38	0	0
9	Fluid friction number	-5.5	-55	-7	70	0.8	8

4.2 Effect of origin of mass movement entering the lake

475
476 We modelled mass movement with a volume of 5×10^6 m^3 entering the lake from the
477 surrounding slopes at various locations identified in section 3.2.3. Our study found that the
478 GLOF process chain initiated by mass movements from locations (Loc-1 to Loc-6) results in a
479 significant fluctuation in the GLOF output (Fig. 4). The peak discharge varied by approximately
480 200%, the total discharge by 55% (Fig. 4). Likewise, the mean flow depth, velocity and arrival
481 time fluctuated by 65%, 82%, 20%, respectively (Table 3). By comparison, the flow resulting
482 from the GLOF initiated by mass entering from the Loc-1 (Fig. 4a) (1 km from the headwall)
483 and Loc-5 (~1.5 km above the left moraine) (Fig. 4e) produced the highest magnitude GLOF
484 and that from the loc-4 (right lateral moraine) (Fig. 4d) was the lowest. For example, the
485 highest peak (180×10^3 m^3) and total discharge (11×10^6 m^3) occurred from Loc-1, while the
486 lowest peak (60×10^3 m^3) and total discharge (7×10^6 m^3) were from Loc-4 (Fig. 4a and 4d).
487 The longest flow reach distance (25 km) was produced by Loc-1 and Loc-5, while the shortest
488 was from Loc-3 (10 km) (Fig. 4c). Solid volumetric portion did not exhibit significant fluctuation,
489 with concentration ranging from 4% (Loc-4) to 5% (Loc-2) (Fig. S3).
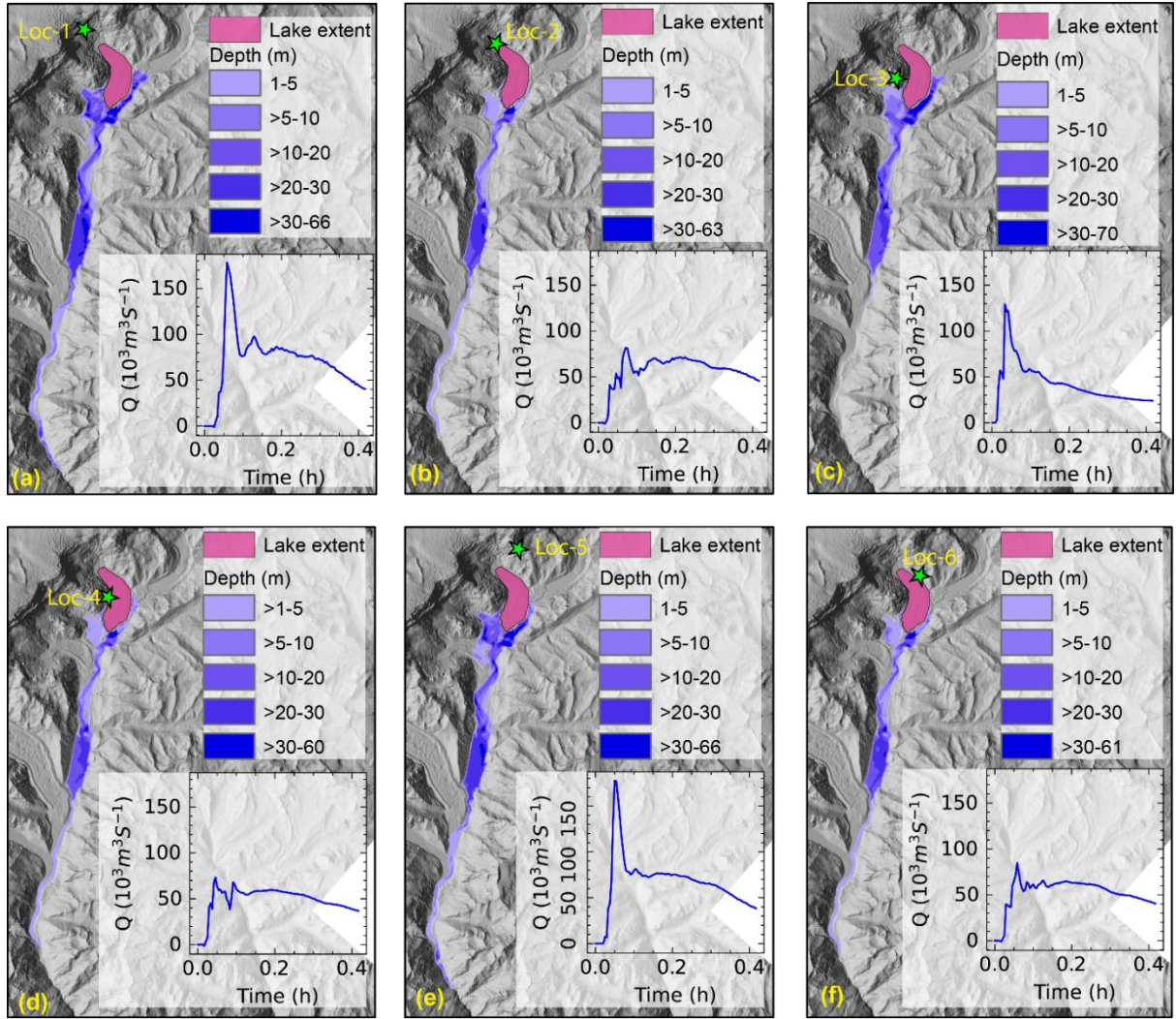
Figure 4: Flow rate and depth resulting from mass movement into the lake from different locations: loc-1 (a) to loc-6 (f).

4.3 Effect of volume and grain density of mass movement entering the lake

To separate the effect of variation in volume V_S and grain density ρS of mass movement entering the lake, we simulated all 10 scenarios of the GLOF event for each volume and density variation using the mass movement initiated from loc-1. Here we observed that only V_S variation leads to a very large variation in the resulting peak (1160%) (Fig. 5a) and total discharge (2500%) (Fig. 6a). Subsequently, this resulted in maximum variation in flow characteristics such as mean flow depth (923%) and flow arrival time (143%) (Table 3, Fig. S3–S6). Conversely, the ρS variation showed the least impact on both peak (5%) and total discharge (24%) (Fig. 5b, 6b, and 7b) and subsequent characteristics such as flow depth (31%) and velocity (2%) (Table 3 and Fig. S3–S6). Both V_S and ρS variation did not result in significant fluctuation in the solid-volumetric concentration of the flow (Fig. S3).
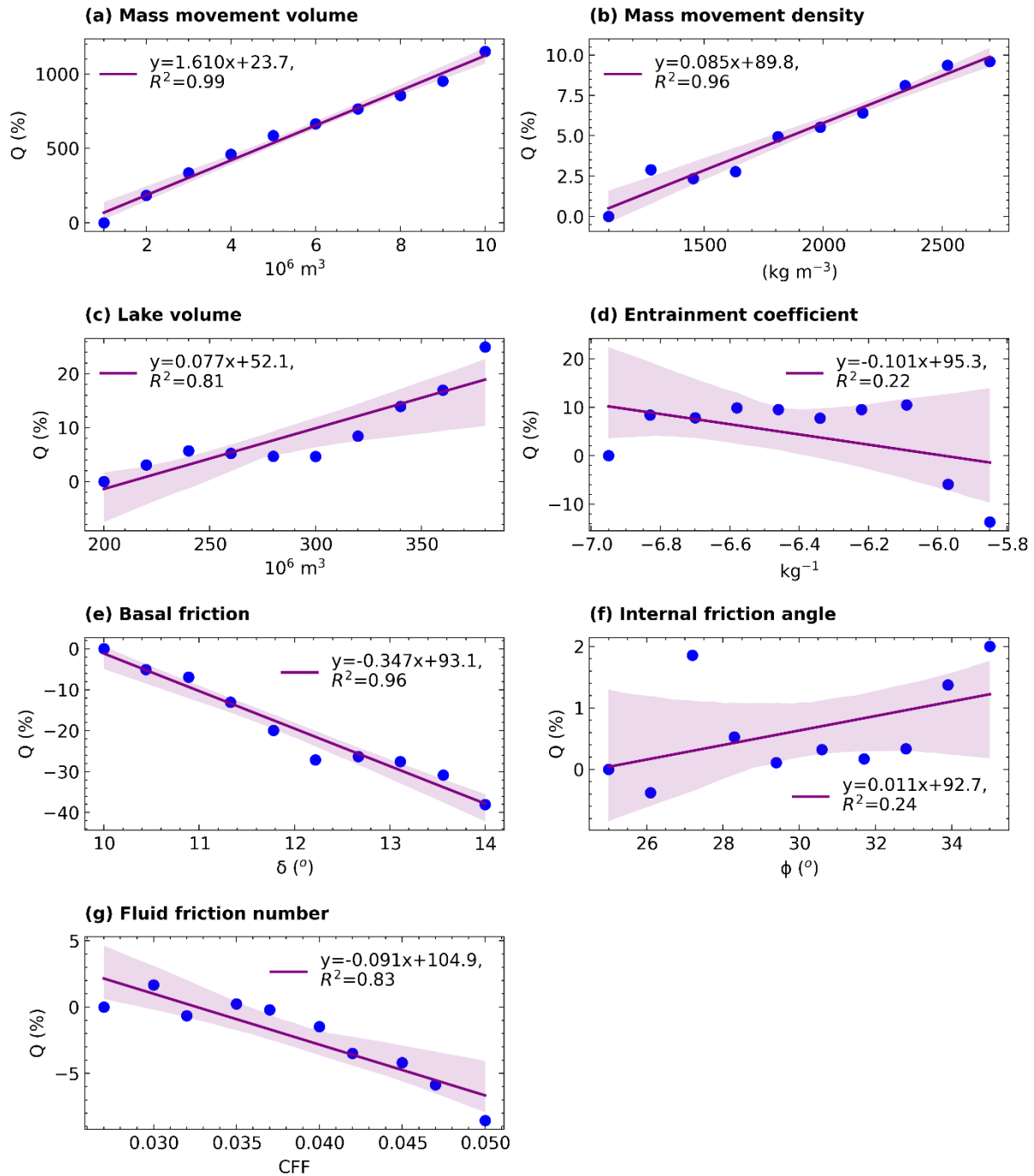
Figure 5: Linear regression between input parameter value variation and percentage change in resulting peak discharge. The linear regression is computed only for the scalable parameters (a) volume of mass movement into the lake, (b) mass movement density (c) volume of glacial lake (d) entrainment coefficient, (e) basal friction angle, (f) internal friction angle and (g) fluid friction number. The shaded envelope around the line shows a 95% confidence interval.
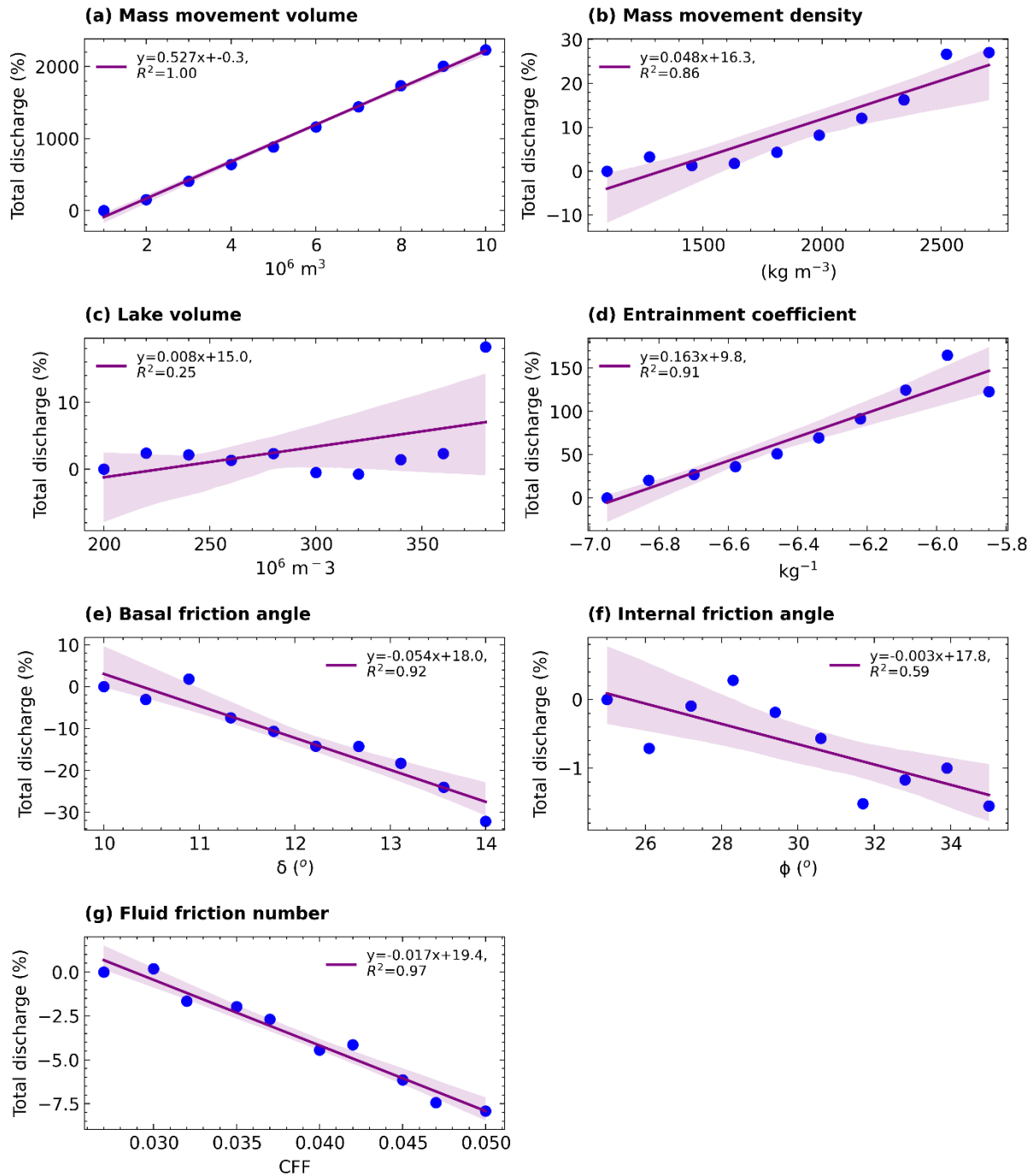
Figure 6: Linear regression between input parameter value variation and resulting total discharge. The linear regression is computed only for the scalable parameters (a) volume of mass movement into the lake, (b) mass movement density (c) volume of the lake (d) entrainment coefficient, (e) basal friction angle, (f) internal friction angle and (g) fluid friction number. The shaded envelope around the line shows a 95% confidence interval.

518 .
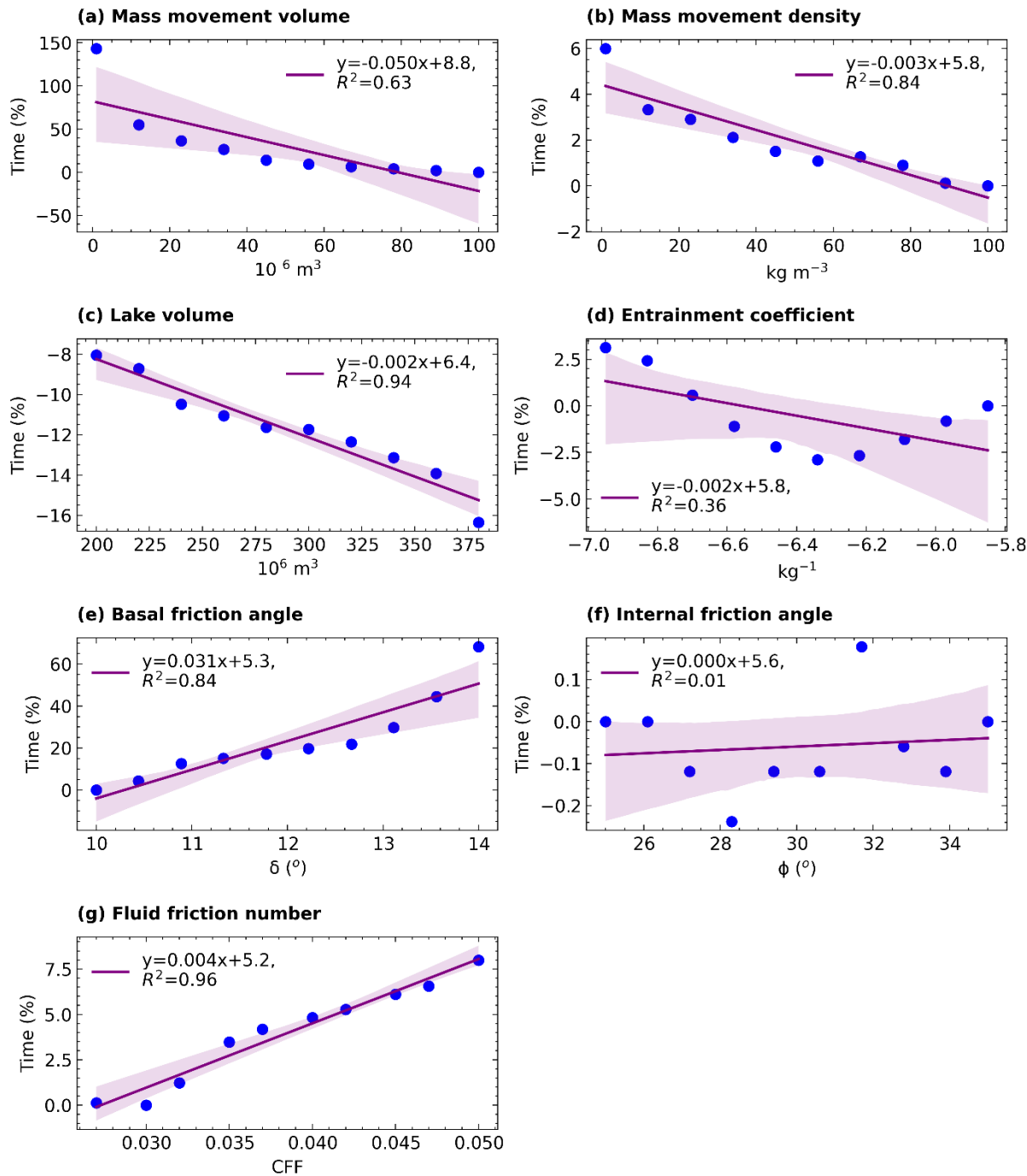
519

520 **Figure 7:** Linear regression between input parameter value variation and flow arrival time.
521 The linear regression is computed only for the scalable parameters (a) volume of mass
522 movement into the lake, (b) mass movement density (c) volume of the lake (d) entrainment
523 coefficient, (e) basal friction angle, (f) internal friction angle and (g) fluid friction number. The
524 shaded envelope around the line shows a 95% confidence interval.

525 **4.4 Lake volume**

Variation in volume of the glacial lake (V_L) from 2 to 3.8 × 10^8, results in total peak discharge variations of 25% with an average of 8.7% (Fig. 5c). Likewise, the total discharge varied by 18% with a mean variation of 3% (Fig. 6c). However, the resulting flow characteristics including flow depth, velocity (Table 3) and arrival time (Fig. 7c) all showed minimal fluctuation, as the total percentage change was well below 10% (Table 3).

4.5 Effect of entrainment coefficient

Variations in the entrainment coefficient (C_E) substantially impact the resulting GLOF output, causing fluctuations in total discharge by 123%, although its impact on peak discharge was minimal (13%) (Fig. 5d and 6d). These changes also affect the flow characteristics including mean depth (49%) and reach distance (20%) (Table 3) but had minimal effect on arrival time (3%) (Fig. 7d). Interestingly, CE variation exhibited threshold effect on peak discharge, total discharge and flow arrival time. The total discharge increases linearly with increasing C_E up to $10^{-5.97}$ kg^{-1} but decreases after this. On the other hand, peak discharge increased when C_E increased from $10^{-6.95}$ to $10^{-6.83}$ kg^{-1}, remained constant between $10^{-6.83}$ kg^{-1} and $10^{-6.09}$ kg^{-1} and decreased from there on. The arrival time decreased when the C_E value was increased from $10^{-6.46}$ kg^{-1} to $10^{-6.46}$ kg^{-1} but increased upon further increase of CE value to $10^{-5.85}$ kg^{-1}. Also, unlike other parameters, entrainment variation affected the solid concentration of the flow (Fig. S3). An increase in the entrainment coefficient from $10^{-6.95}$ to $10^{-5.85}$ kg^{-1} led to a 30% increase in the mean solid volumetric concentration of the flow.

4.6 Effect of frictional parameters

Among the frictional parameters, basal friction angle (δ) resulted in a significant fluctuation in GLOF magnitude (Fig. 5e, 6e, 7e) and subsequent flow characteristics (Fig. S3–S6). While the variation of fluid friction number (C_{FF}) had minimal impact on the resulting peak and total flow (Fig. 5g, 6g), it notably altered other flow characteristics, such as flow velocity (55%) and depth (70%) (Table 3). The increase of δ from 10 to 14° resulted in a peak and total discharge decrease of 36% (Fig. 5d) and 32% (Fig. 6d), respectively. Likewise, the flow velocity decreased by 23% resulting in a delay in flow arrival by 68% (Table 3). Conversely, the peak flow decreased by 2% only in response to an increase in the internal friction angle (ϕ) from 25-35˚ (Fig. 5f). The variation in all frictional parameter values did not result in a significant change in the solid volumetric concentration of the flow (Fig. S5).
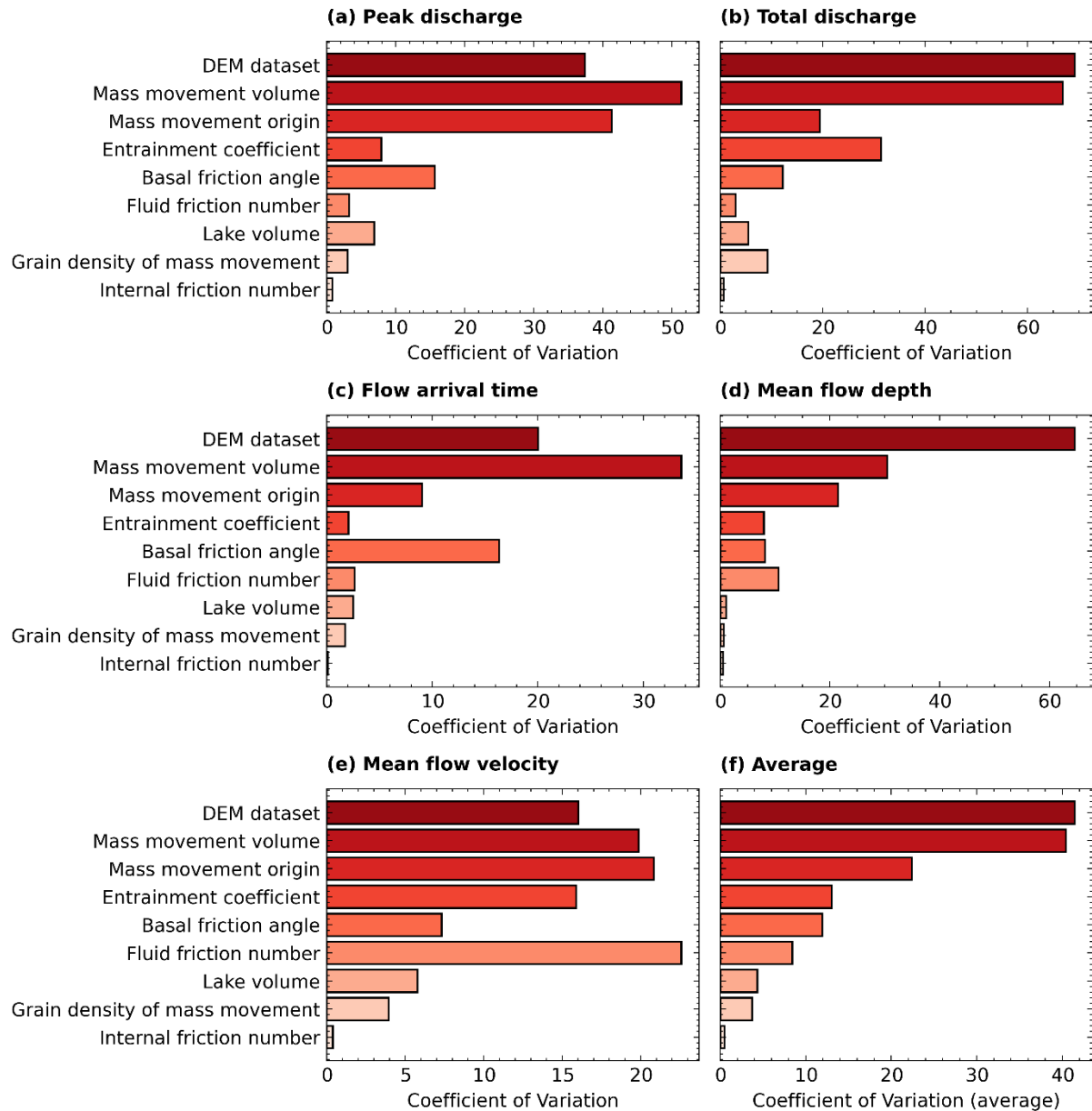
Figure 8: The coefficient of variation for (a) peak flow, (b)volume, (c) time, (d) average flow depth along the river centreline, (e) flow velocity along the river centreline and (f) average across all these output parameters.

4.7 Comparison of the effects of all parameters

To compare output sensitivity resulting from all input parameters considered here, we calculated the percentage of coefficient of variation (CV) for peak flow, total discharge, arrival time, flow depth and flow velocity. We further computed the average CV (avg. CV) across all these output variables and examined the overall impact of each input parameter variation. Comparing all these output indicators, V_S had the greatest impact (avg. CV = 47%), followed by DEM datasets (avg. CV = 35%) and the origin of mass movement (avg. CV = 21%). Other input parameters like δ and C_E also caused significant variation in resulting GLOFs. Notably,

568   C_{FF} significantly impacted flow depth with its CV = 16% despite having minimal impact on other

569   flow characteristics.

570   For the seven scalable parameters, we computed linear regression (Fig. 5–7). The linear

571   regression analysis revealed that the five parameters: V_S (R^2 = 0.99), ρS (R^2=0.96), V_L (R^2 =

572   0.81), δ (R^2 = 0.96) and C_{FF} (R^2 = 0.83) demonstrated strong explanatory power in accounting

573   the variability in GLOF peak discharge (Fig. 5). Among these sets of parameters, V_S (m = 1.6),

574   ρS (m = 0.085) and V_L (m = 0.07), showed a positive relationship while δ (m = -0.347), C_E (m=-

575   0.091) and C_{FF} (m = -0.09) exhibited a negative relationship (Fig. 5). All seven parameters

576   (R^2 >0.86) except for the ϕ (R^2 =0.59) and V_L (R^2= 0.25) indicated a high level of explanatory

577   power regarding the variation of resulting total discharge (Fig. 6). Comparing all seven input

578   parameters, V_S exhibited the highest R^2 value for both peak and total discharge, signifying a

579   strong explanatory power regarding the modelled flow compared to the other parameters.

580   Additionally, the rate of change of peak discharge and total discharge for every unit increase

581   in V_S was comparatively higher than other parameters as indicated by the steepness of the

582   slope (Fig. 5a and 6a).

583   Basal friction angle and C_{FF} demonstrated a high level of explanatory power concerning the

584   variability in flow arrival time, as evidenced by their R^2 values of 0.98 and 0.97, respectively.

585   Mass movement volume variation also exhibited a high explanatory power with a negative

586   relationship, with R^2 of 0.81 and a slope (m) of -0.019. However, the linearity became less

587   pronounced within the volume range of 4×10^6 m^3 to 10×10^6 m^3. In contrast, other

588   parameters, including C_E, and ϕ, did not exhibit a definitive linear relationship (Fig. 7).

589   However, C_E variation showed a threshold effect on arrival time; increasing the C_E from $10^{-5.95}$

590   to $10^{-6.42}$ kg^{-1} decreased arrival time, while further increases towards $10^{-5.85}$ kg^{-1} led to a linear

591   increase in arrival time.

592   **5 Discussion**

593   Our primary aim was to investigate the sensitivity of the modelled GLOF outputs to a range of

594   values for key model input parameters using r.avaflow model. Previous studies have

595   underscored the sensitivity of GLOF model outputs to some input parameters, including basal

596   friction angle, entrainment coefficient and volume of mass movement entering the lake (Baggio

597   et al., 2021; Mergili et al., 2018b; Mergili et al., 2020a). This study advances our understanding

598   of GLOF modelling by conducting a comprehensive sensitivity analysis across nine essential

599   parameters and multiple (84) GLOF simulations. As a result, we have for the first time, ranked

600   these nine GLOF input parameters based on their contributions to model output variabilities.

601   Our results showed that modelled GLOF output parameters are substantially sensitive to five

602 of the nine parameters we tested here (DEM dataset, volume of mass movement into the lake,
603 origin of mass movement into the lake, entrainment coefficient, and basal friction angle)
604 suggesting that GLOF modelling results are subject to uncertainty from multiple sources. The
605 findings offer valuable perspectives on the uncertainty of GLOF modelling results and
606 complexities inherent in modelling the GLOF process chain within the rugged mountain terrain
607 such as in the Himalaya.

5.1 DEM datasets

609 DEM is one essential data for GLOF and other flood modelling (Hawker et al., 2018; Saksena
610 and Merwade, 2015; Schumann and Bates, 2018; Westoby et al., 2014). The impact of DEM
611 resolution is even more pronounced in the steep and complex topographic conditions
612 prevalent in high mountain regions like the Himalaya (Liu et al., 2019). Our study provides the
613 quantification of the effect of DEM in such environments for the first time. Our results suggest
614 that the use of global and regional DEM datasets with resolution ranging from 8 m (HMA-DEM)
615 to 90 m (SRTMGL3) leads to over two-fold and four-fold variations in peak and total discharge,
616 respectively, and cause successive significant fluctuations in flood height, reach distance and
617 flow arrival time. This likely results from the low-resolution DEMs not fully resolving the river
618 channel compared to higher-resolution DEMs. This limitation results in a reduction in surface
619 roughness and river channel conveyance (carrying capacity of channel). Thus, the flow
620 spreads out more, leading to an increase in the modelled flow extent and reach (Fig. 9 and
621 Fig. S7) (Muthusamy et al., 2021). This was supported by comparing the DEM profile and flow
622 depth along the river centreline (Fig. 9) and across the multiple vertical cross-sections along
623 the river channel (Fig. S6). The analysis showed that GLOF output from SRTMGL3, where
624 river channels are poorly resolved, was comparatively higher than that from the HMA-DEM
625 with the better-resolved channel. Also, DEM datasets were acquired at different times,
626 meaning the topographic features they captured will also differ depending on natural
627 geomorphological change or human-made alteration of the earth's surface over time (Khosh
628 Bin Ghomash et al., 2019; Bishop et al., 2002; Schumann and Bates, 2018; Watson et al.,
629 2015). Such discrepancies will have a substantial influence on flow characteristics and huge
630 uncertainty if a DEM with inadequate spatial and temporal resolution is used in GLOF
631 modelling.

632
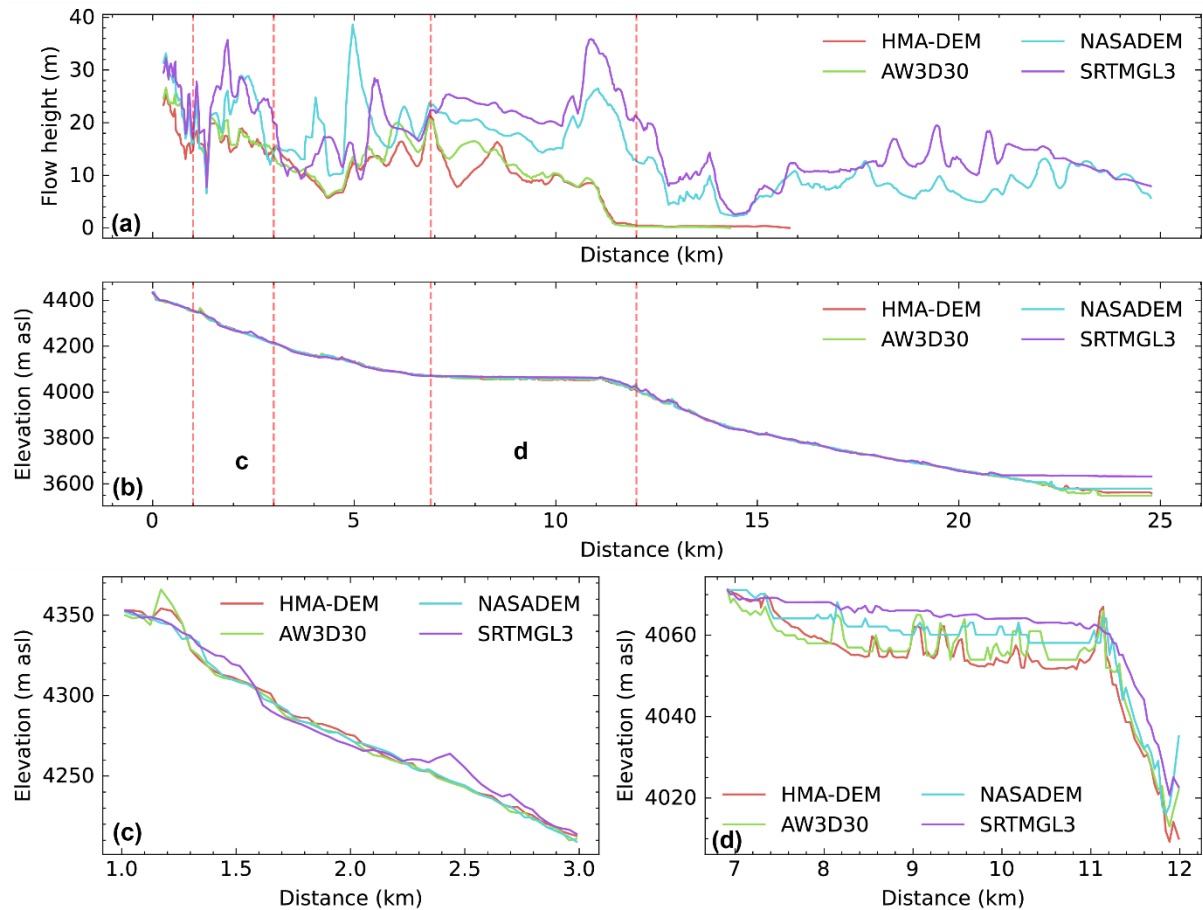
Figure 9: A comparison of the elevation profiles from four DEM datasets and the corresponding flow depths along the river centreline, generated through r.avaflow modelling. panels (a) and (b) show the flow depths and elevation profiles along the river centreline. Panels (c) and (d) illustrate elevation profiles for two specific sections marked in (a) and (b). DEM and flow depth profiles from the vertical cross sections at various distances are also provided in the supplementary figure (Fig. S6). The DEM datasets were co-registered using the algorithm developed by Shean et al. (2016).

Overestimation of flood maps stemming from reductions in DEM resolution has been reported in urban flood modelling (Muthusamy et al., 2021; Mcclean et al., 2020). However, the impact of DEM data on GLOF modelling, especially in a complex topographic setting such as in the Himalaya has been rarely documented (Wang et al., 2011). Our results show the substantial variation in GLOF model output stemming from DEM dataset variation, even when employing DEM with comparable spatial resolutions, underscores the criticality of high-quality DEM data in GLOF modelling (Fig. 9). DEM datasets covering rugged high mountain terrain, where GLOFs typically occur are likely to have more errors due to geometric distortion and data loss due to challenges involved in data acquisition for DEM production (Hugonnet et al., 2021; Liu et al., 2019). Therefore, using global to regional scale open-access DEMs, such as SRTM for GLOF modelling due to the absence of high-resolution alternatives (Wang et al., 2011) may

651 only be suitable for first-order assessment of GLOFs at large scales (Zhang et al., 2023b).
652 This is important as uncertainty stemming from DEM datasets is often overlooked and/or not
653 well addressed in the previous basin-specific GLOF modelling work (Rinzin et al., 2023; Sattar
654 et al., 2023; Sattar et al., 2021b).

5.2 Mass movement origin variation

656 Our study indicated that different origin of mass movement initiation produced GLOFs with
657 approximately two-fold variations in their peak discharge, volume, and reach distance (Fig. 4).
658 These variations can be explained based on the lake geometry and the direction, horizontal
659 distance and vertical distance at which the mass movement enters the lake. r.avaflow model
660 provides detailed output parameters such as kinetic energy associated with the flow, and flow
661 depth map for each time step, which allowed us to better understand the cause of this
662 variation. For example, the mass movement originating from Loc-1, which is located at the
663 slope above the headwall, directly impacts the head end of the lake with the highest kinetic
664 energy (50714 GJ) among all other sources of mass movement. This head-end impact,
665 coupled with its high energy, facilitates the direct forward propagation of waves toward the
666 frontal outlet, causing the lake water to overtop the frontal moraine and resulting in a higher
667 peak and total discharge (Fig. S7). Thorthormi Tsho is roughly crescentic in shape and curves
668 toward the west, with its maximum curvature facing the mass movement origin of Loc-5. This
669 shape also allows the impact wave generated from mass movement from Loc-5 to move
670 almost unimpeded along the flow line, resulting in greater GLOF discharge. Also, Loc-1 and
671 Loc-5 are located at greater distances and higher elevations from the lake compared to other
672 locations (Fig. 2). This spatial location might have also enabled them to generate greater force
673 to impact the lake. In contrast, the direct wave of impact generated by the mass movement
674 from Loc-3, located on the slope above the right moraine dam, is deflected towards the left
675 lateral moraine, and only a secondary wave proceeds towards the lake outlet, resulting in a
676 comparatively lower peak and total discharge (Fig. S7) (Emmer et al., 2024). This finding
677 implies that the geometry of the glacial lake and the surrounding source slope plays a vital
678 role in GLOF output. Thus, we underscore the importance of considering catchment shape in
679 GLOF modelling, although we cannot assume that two identical basins will have the same
680 flood properties due to the influence of other factors, such as the involved volume of solid and
681 fluid parts.

682 Earlier studies (Mergili et al., 2017; Mergili et al., 2020b) have explained the interaction
683 between landslides and reservoirs (lakes) and their influence on the resulting hydrograph.
684 However, these studies did not consider the variables such as directions and distances from
685 which the mass impacts the lake. To fill this gap, here we enhanced our understanding of the

686   interplay between the resulting GLOF magnitude and mass movement attributes including the

687   direction and distance from which the mass enters the lake, the amount of kinetic energy the

688   mass possesses and the geometry of the lake. Our results emphasize the significant impact

689   on the resulting GLOF events caused by the uncertainty in pinpointing the specific location of

690   origin of mass movement into the lake. Thawing of permafrost and destabilization of the slope

691   surrounding the lake due to climate warming (Gruber et al., 2017; Kääb et al., 2018; Sattar et

692   al., 2025) combined with the expansion of the glacial lake towards the mountain flank (Rounce

693   et al., 2016) are likely to increase the frequency of mass movement into the lake, further

694   exacerbating this uncertainty. By effectively identifying and quantifying the uncertainties

695   related to the origin of mass movement entering the lake in addition to the volume, we propose

696   considering the origins of mass movement in designing the scenario-based GLOF modelling

697   in future studies. This approach goes beyond the existing practice, which primarily focuses on

698   the volume of mass movement entering the lake. This is important because, as demonstrated

699   in our study, the impact of mass movement can vary significantly depending on its origin. In

700   some cases, what may be considered a worst-case scenario from one origin might represent

701   only a low-magnitude event from another (Gaphaz, 2017; Sattar et al., 2021a; Allen et al.,

702   2022).

703   **5.3 Mass movement volume, grain density, entrainment coefficient, and lake volume**

704   Our investigation revealed that variation in GLOF magnitude is most sensitive to the volume

705   of mass movement (V_S) entering the lakes. It also exhibits a significant level of sensitivity to

706   the entrainment coefficient (C_E) whilst the grain density (ρS) and lake volume (V_L) exhibit

707   negligible impact. For example, the variation of V_S between 1×10^6 m^3 and 10×10^6 m^3 leads to

708   peak and total discharge fluctuation of 1160% and 2500%, respectively, and subsequent

709   variation in maximum flow depth and arrival time (Fig. 5 to Fig. 7). The dominant impact of V_S

710   and C_E on GLOF magnitude could be due to their direct influence on the overall magnitude

711   and intensity of flood events. The total discharge during the GLOF cascade event is a function

712   of the V_S entering the lake. This is further corroborated by the near-perfect linear relationship

713   of peak discharge ($R^2 = 0.99$) and total discharge ($R^2 = 1$) with the V_S entering the lake

714   observed here. Likewise, the volume of solid content in the flow is solely contributed by the

715   entrainment of frontal moraine material, primarily determined by the C_E. Additionally, this

716   correlation could be attributed to the amount of energy and associated momentum of the flow,

717   which changes significantly with corresponding variations in V_S. Also, it could be due to the

718   longer timing and duration of the flow as evident in Fig. S2. Most GLOF events in high

719   mountains across the HMA and other alpine regions are caused by moraine dam breaches

720   triggered by mass movement entering the lake from the surrounding mountain flank (Shrestha

et al., 2023; Lützow et al., 2023; Emmer and Vilímek, 2014). As a result, V_S is considered a primary basis for scenario development (Allen et al., 2022). Thus, we believe this finding provides useful insights towards improving the development of different scenarios of GLOFs with higher confidence, or is a basis for ensemble testing, with the caveat that the range of outputs may be too wide to be of practical use.

The volume of a glacial lake is one of the key parameters in GLOF modelling and subsequent hazard mapping. Without field-measured bathymetry, we applied eight different empirical equations to estimate the volume of Thorthormi Tsho, which ranged between 2.1 and 3.80 × 10^8 m³. Interestingly, this variation in V_L did not significantly influence the modelled GLOF hydraulics; V_L was ranked as the third least sensitive parameter in our analysis. This limited impact may be attributed to the large size of Thorthormi Tsho (~4.35 km²) and its substantial storage capacity, as estimated by the empirical equations. Even the lower bound of the calculated V_L exceeds 95% of the measured volume of the glacial lake and the upper bound is greater than 58 of the 59 measured volume of the lake in the greater Himalaya (Zhang et al., 2023a). We believe that the Thorthormi Tsho's large volume and expansive area enable it to absorb and dissipate the energy from potential mass movement impacts, effectively acting as a buffer (Emmer et al., 2024). Nevertheless, while our findings suggest that V_L uncertainty may have a relatively minor impact on GLOF modelling for large lakes like Thorthormi Tsho, we acknowledge that V_L remains a critical parameter in GLOF modelling, particularly for smaller lakes where volume changes could have a more pronounced effect on flood dynamics (Sattar et al., 2023).

5.4 Frictional parameters variations

Among the frictional parameters, our result showed that GLOF magnitude is most sensitive to the basal friction angle (δ). For example, the variation of total discharge (47.5%) resulting from fluctuation of δ within the experiment range was 30 times greater than that of internal friction angle (φ) and over four times greater than that of fluid friction angle (C_{FF}). δ plays a dominant role in flow dynamics and the interaction between the flowing material and the channel bed. This direct contact means that even minor changes in δ can have substantial effects on the resistance encountered by the flowing material, thereby influencing the mobility of the flow (Pudasaini and Krautblatter, 2014a; Mergili et al., 2018a; Mergili et al., 2018b). φ on the other hand primarily affects particle interactions within the flowing material, whilst C_{FF} is a coefficient which quantifies the overall flow resistance within the flow path mainly depending on surface roughness. Our findings indicate that prioritizing the consideration of δ over the other two frictional parameters is advisable. While the back-calculated values might seem reasonable initiation values for δ as measuring it in the field is practically not feasible we recommend

conducting a statistical substantial sensitivity analysis using adequate sampling size and an appropriate statistical model. Despite the relatively low overall impact on GLOF magnitude, the C_{FF} notably increased the flow's mobility, especially beyond 12 km downstream, when the flow became fluid-dominant (Fig. S4). This is because C_{FF} controls the mobility of the fluid part (Mergili and Pudasaini, 2024; Mergili et al., 2017). This suggests that C_{FF} could exert a substantial influence, particularly in modelling scenarios encompassing longer flow distances.

5.5 Key points from the comparison of all parameters and the way forward

Identifying the most accurate parameter values or optimal datasets can be achieved through validation with well-constrained historical events (Zheng et al., 2021a; Schneider et al., 2014; Mergili et al., 2020b; Shugar et al., 2021; Sattar et al., 2025), but there are limitations in the transferability of these findings due to unique characteristics and initial conditions of each GLOF, such as varying proportions of solid and liquid parts. Because of this we effectively constrained how variation in input parameter values within commonly used ranges, influences the GLOF modelling results, instead of trying to determine the 'correct' value for each parameter. Or, put another way, if we apply our study to a specific example, we may determine that certain factors are more important than others for this specific example, but it would be unclear how applicable our results are to other events. Thus, we see our approach as the least biased towards any particular event and hence the most generally applicable approach. Our results indicating modelled GLOF being subjected to uncertainty from multiple input parameters implies that parameter value determined from one modelled GLOF event might not accurately predict the behaviour of GLOFs in different regions or under different circumstances (Mergili et al., 2018a; Mergili et al., 2020b). Therefore, while these back-analysed parameter values can provide valuable insights, they need to be applied with caution and adapted to the specific context of each new GLOF scenario. As a result of these multiple sources of uncertainty in modelled GLOF, it could pose challenges in effectively communicating risks with communities and other stakeholders (Thompson et al., 2020). We highlight that more sensitive parameters should be treated carefully in future GLOF modelling works by robustly considering associated uncertainties.

Due to the high sensitivity of the model output on DEM resolution, we emphasize the critical importance of high-resolution and good-quality DEM (Uuemaa et al., 2020; Schumann and Bates, 2018), especially when modelling is aimed at producing hazard maps with higher granularity at the specific basin scale. DEMs should be high spatial resolution, high vertical accuracy and recently produced, especially in areas of high relief and rapid landscape change such as in Himalaya (Schumann and Bates, 2018). Previous studies have indicated that flood modelling accuracy can be improved by correcting the effect of DEM resolution and accuracy

791 (Saksena and Merwade, 2015) or by merging with other high-resolution and accurate DEMs

792 (Muthusamy et al., 2021). These methods appear viable in the context of highly sparse

793 coverage of high-resolution DEMs and the unaffordability of high-resolution commercial

794 DEMs, but the modelling results may be subjected to substantial uncertainty.

795 Mass movement volume and δ exhibit a strong linear relationship with all output parameters.

796 Whilst the linear relationship does not negate the influence these parameters have on flow

797 characteristics; it suggests that model output errors resulting from uncertainties in these

798 parameters might be predictable. This is essential since predicting the V_S movement involved

799 in the forward modelling is highly challenging and determining an accurate value is impossible

800 – the current challenge is rather to establish a likely envelope of volumes. However, such

801 prediction should be bespoke to the particular events based on the initial parameters like

802 estimated ice thickness, slope, and presence of permafrost. Furthermore, such predictions

803 must also consider other factors, such as equifinality arising from the interaction of multiple

804 parameters (Mergili et al., 2018a; Mergili et al., 2018b; Mergili et al., 2020b).

805 The entrainment coefficient exhibits a threshold effect for peak discharge, arrival time and total

806 discharge but these thresholds occur at different C_E values for each of these output

807 parameters. The observed threshold effects in flow characteristics can likely be attributed to

808 the initial dominance of the fluid component, wherein the contribution of erosion to the flow

809 dynamics is negligible. As the erosion rate progresses with increasing CE values, the

810 increasing concentration of eroded material reduces the mobility of the flow, leading to a

811 decline in mobility of the flow. These threshold effects suggest that once these thresholds are

812 surpassed, the resulting flow and arrival time demonstrate a heightened sensitivity to

813 variations in entrainment. Consequently, this sensitivity may translate to the flow

814 characteristics such as flow depth and arrival time which are essential for hazard and risk

815 assessments. It is important to note that this threshold value may vary across different GLOF

816 events due to the diverse combinations of other parameters.

817 The GLOF simulations were conducted using the r.avaflow model due to its capability to model

818 the entire GLOF process chain (Mergili and Pudasaini, 2024; Mergili et al., 2017). While we

819 present the uncertainty involved in the full process chain GLOF from mass movement entering

820 the lake to downstream propagation, we specifically explored the uncertainty of the GLOF

821 input parameters relevant to r.avaflow modelling. Input parameters such as DEM datasets,

822 and the volume and density of mass movement involved in a GLOF event, might be similar

823 across different models. However, it should be noted that all parameters tested here do not

824 necessarily apply to all models used for GLOF modelling.

825   The flow arrival time was measured from the profile located 3 km, 6 and 9 km downstream of
826   the lake since some of our modelled GLOF terminates before proceeding further downstream.
827   This is a reasonable point as human settlement downstream of the lake is mostly concentrated
828   around this area. The variation of flow arrival time might be underestimated if the location is
829   farther downstream from the lake.

830   Here we focused on nine essential parameters in r.avaflow, which are relevant to GLOF
831   modelling. As an open-source modelling code, r.avaflow model offers flexibility by allowing
832   the users to manipulate all parameters, a level of transparency that sets it apart from many
833   modelling codes. However, including inbuilt modules, initial conditions, and all flow
834   parameters, r.avaflow has more than 30 tuneable parameters (Mergili and Pudasaini, 2024)
835   (Table S1). Our choice of parameter in this study is essentially motivated by those identified
836   as critical and commonly modified in the previous GLOF modelling studies and which are
837   frequently modified to fit with the parameter from back-calculated events. Because of this, our
838   sensitivity analysis might have potentially overlooked the complexity of r.avaflow stemming
839   from the effect of all these parameters, let alone their interaction effect. Also due to the
840   enormous computational time and resources required for running r.avaflow, we used one-at-
841   a-time sensitivity analysis conducting up to 10 simulations per parameter. While this number
842   of simulations for each parameter produced substantially conclusive results, we do not
843   discount the robustness of global sensitivity analysis employing an adequate sampling size
844   which can adequately account for the influence of parameter interactions (Saltelli et al., 2004).
845   While we offer for the first time the importance of considering the uncertainty of these
846   parameters in GLOF modelling, in the light of all these limitations, we provide the following
847   recommendations: 1) We recommend that future studies include a broader range of
848   parameters, further advancing the understanding of their roles in GLOF modelling: 2) This
849   can be achieved by initially focusing on the most sensitive parameters identified in this study
850   and progressively expanding the analysis to include other parameters. Adequate sample sizes
851   and appropriate statistical models should be employed to ensure robust findings: 3) Given that
852   r.avaflow is an open-source tool under continuous development, we underscore the
853   implementation of features that support parallel computation for parameter interaction
854   analyses. This advancement would enable future studies to fully utilize high-performance
855   computing (HPC) resources and address complex modelling challenges more effectively.

856   **6 Conclusions**

857   GLOFs present substantial dangers to communities residing in valleys downstream of glacial
858   lakes. GLOFs involve complex cascading processes and typically occur across rugged
859   mountain terrains. Due to these complexities, modelling GLOFs necessitates extensive input

860   data, parameters, and complex modelling codes for accurate hazard and risk assessments,

861   which is inherently challenging. However, previous studies have mostly relied on open-access

862   data and are grounded in a historical event introducing significant uncertainties to the

863   modelling results. In this study, we have, for the first time, conducted sensitivity analysis

864   considering multiple GLOF parameters and ranked these inputs based on how their

865   uncertainties in input values apportion to the variation in modelling output, by employing

866   cutting-edge modelling code, r.avaflow. Our results suggested GLOF modelling outputs such

867   as peak and total discharge are substantially sensitive to variation in input values of six out of

868   nine parameters we tested here. Specifically, the modelling outputs are the most sensitive to

869   the volume of mass movement entering lakes followed by the variation in DEM datasets and

870   the location of origin of mass movement entering the lake. Other parameters like, basal

871   frictional angle and entrainment coefficient also showed significant sensitivity. Although limited

872   to GLOF modelling with the r.avaflow model, our study emphasizes that GLOF modelling

873   results are influenced by uncertainties stemming from various sources, underscoring the need

874   for careful interpretation of the modelling results. By ranking the model parameters according

875   to their impact on model output, our study prioritizes model input parameters for future

876   modelling efforts, given the challenge of adequately constraining multiple parameters.

877   Additionally, this study lays the groundwork for a thorough investigation into the most sensitive

878   parameters, to improve our understanding of GLOF modelling.

Acknowledgement

880   This work was supported by the Natural Environment Research Council (NERC)- funded

881   IAPETUS Doctoral Training Partnership [IAP2-21-267]. We thank Dr. Sonam Wangchuk of

882   ICIMOD for helping us in setting experiments in the HPC.

Code and data availability

884   The r.avaflow modelling code we used here for simulating all scenarios of GLOF can be

885   accessed at: r.avaflow | The mass flow simulation tool (landslidemodels.org). The SRTMGL3,

886   NASADEM and AW3D30 DEMS used here can be downloaded from the OpenTopogragphy

887   at: OpenTopography - Find Topography Data. The HMA-DEM can be downloaded from the

888   National Ice and Snow Data Center at: High Mountain Asia 8-meter DEM Mosaics Derived

889   from Optical Imagery, Version 1 | National Snow and Ice Data Center (nsidc.org).

Supplement

891   The supplement related to this article is available online at:

Author contributions

SR, SA and RC conceptualized the study. SR undertook the data and data processing and analysis. SA and RC secured the funding, supervised, and contributed equally to the work. AS helped modelling and was involved as an external supervisor. MM revised and provided an expert opinion on the study. All authors wrote and revised the manuscript.

Competing interests

The contact author declares that none of the authors has any competing interests.

References

(SRTM), N. S. R. T. M.: Shuttle Radar Topography Mission (SRTM) Global [dataset], https://doi.org/10.5069/G9445JDF, 2013.

Abdi, H.: Coefficient of variation, Encyclopedia of research design, 1, 2010.

Allen, S. K., Zhang, G., Wang, W., Yao, T., and Bolch, T.: Potentially dangerous glacial lakes across the Tibetan Plateau revealed using a large-scale automated assessment approach, Science Bulletin, 64, 435-445, 10.1016/j.scib.2019.03.011, 2019.

Allen, S. K., Linsbauer, A., Randhawa, S. S., Huggel, C., Rana, P., and Kumari, A.: Glacial lake outburst flood risk in Himachal Pradesh, India: an integrative and anticipatory approach considering current and future threats, Natural Hazards, 84, 1741-1763, 10.1007/s11069-016-2511-x, 2016.

Allen, S. K., Sattar, A., King, O., Zhang, G., Bhattacharya, A., Yao, T., and Bolch, T.: Glacial lake outburst flood hazard under current and future conditions: worst-case scenarios in a transboundary Himalayan basin, Natural Hazards and Earth System Sciences, 22, 3765-3785, 10.5194/nhess-22-3765-2022, 2022.

Baggio, T., Mergili, M., and D'Agostino, V.: Advances in the simulation of debris flow erosion: The case study of the Rio Gere (Italy) event of the 4th August 2017, Geomorphology, 381, 10.1016/j.geomorph.2021.107664, 2021.

Bishop, M. P., Shroder, J. F., Bonk, R., and Olsenholler, J.: Geomorphic change in high mountains: a western Himalayan perspective, Global and Planetary Change, 32, 311-329, https://doi.org/10.1016/S0921-8181(02)00073-5, 2002.

Buckley, S., Agram, P., Belz, J., Crippen, R., Gurrola, E., Hensley, S., Kobrick, M., Lavalle, M., Martin, J., and Neumann, M.: NASADEM, National Aeronautics and Space Administration, Jet Propulsion Laboratory, California Institute of Technology: Pasadena, CA, USA, 2020.

Byers, A. C., Rounce, D. R., Shugar, D. H., Lala, J. M., Byers, E. A., and Regmi, D.: A rockfall-induced glacial lake outburst flood, Upper Barun Valley, Nepal, Landslides, 16, 533-549, 10.1007/s10346-018-1079-9, 2018.

Carrivick, J. L. and Tweed, F. S.: A global assessment of the societal impacts of glacier outburst floods, Global and Planetary Change, 144, 1-16, 10.1016/j.gloplacha.2016.07.001, 2016.

Dubey, S. and Goyal, M. K.: Glacial Lake Outburst Flood Hazard, Downstream Impact, and Risk Over the Indian Himalayas, Water Resources Research, 56, 10.1029/2019wr026533, 2020.

Dubey, S., Sattar, A., Goyal, M. K., Allen, S., Frey, H., Haritashya, U. K., and Huggel, C.: Mass Movement Hazard and Exposure in the Himalaya, Earth's Future, 11, 10.1029/2022ef003253, 2023.

Emmer, A. and Cochachine, L.: The causes and mechanisms of moraine-dammed lake failures in the Cordillera blanca, North American Cordillera, and Himalayas, AUC Geographica, 48, 10, 2013.

Emmer, A. and Vilímek, V.: New method for assessing the susceptibility of glacial lakes to outburst floods in the Cordillera Blanca, Peru, Hydrology and Earth System Sciences, 18, 3461-3479, 10.5194/hess-18-3461-2014, 2014.

Emmer, A., Vilca, O., Salazar Checa, C., Li, S., Cook, S., Pummer, E., Hrebrina, J., and Haeberli, W.: Causes, consequences and implications of the 2023 landslide-induced

Lake Rasac GLOF, Cordillera Huayhuash, Peru, EGUsphere [preprint], 10.5194/egusphere-2024-2316, 2024.

Farinotti, D., Huss, M., Fürst, J. J., Landmann, J., Machguth, H., Maussion, F., and Pandit, A.: A consensus estimate for the ice thickness distribution of all glaciers on Earth, Nature Geoscience, 12, 168-173, 10.1038/s41561-019-0300-3, 2019.

Frey, H., Huggel, C., Chisolm, R. E., Baer, P., McArdell, B., Cochachin, A., and Portocarrero, C.: Multi-Source Glacial Lake Outburst Flood Hazard Assessment and Mapping for Huaraz, Cordillera Blanca, Peru, Frontiers in Earth Science, 6, 10.3389/feart.2018.00210, 2018.

Fujita, K., Sakai, A., Takenaka, S., Nuimura, T., Surazakov, A. B., Sawagaki, T., and Yamanokuchi, T.: Potential flood volume of Himalayan glacial lakes, Natural Hazards and Earth System Sciences, 13, 1827-1839, 10.5194/nhess-13-1827-2013, 2013.

950 Gantayat, P., Sattar, A., Haritashya, U. K., Watson, C. S., and Kargel, J. S.: Bayesian Approach to
951 Estimate Proglacial Lake Volume (BE-GLAV), Earth and Space Science, 11, 10.1029/2024ea003542,
952 2024.
953 GAPHAZ: Assessment of Glacier and Permafrost Hazards in Mountain Regions. Technical Guidance
954 Document, Standing Group on Glacier and Permafrost Hazards in Mountains (GAPHAZ) of the
955 International Association of Cryospheric Sciences (IACS) and the International Permafrost Association
956 (IPA). 72, 2017.
957 Gruber, S., Fleiner, R., Guegan, E., Panday, P., Schmid, M.-O., Stumm, D., Wester, P., Zhang, Y., and
958 Zhao, L.: Review article: Inferring permafrost and permafrost thaw in the mountains of the Hindu
959 Kush Himalaya region, The Cryosphere, 11, 81-99, 10.5194/tc-11-81-2017, 2017.
960 Hawker, L., Bates, P., Neal, J., and Rougier, J.: Perspectives on Digital Elevation Model (DEM)
961 Simulation for Flood Modeling in the Absence of a High-Accuracy Open Access Global DEM, Frontiers
962 in Earth Science, 6, 10.3389/feart.2018.00233, 2018.
963 Huggel, C.: Recent extreme slope failures in glacial environments: effects of thermal perturbation,
964 Quaternary Science Reviews, 28, 1119-1130, 10.1016/j.quascirev.2008.06.007, 2009.
965 Hugonnet, R., McNabb, R., Berthier, E., Menounos, B., Nuth, C., Girod, L., Farinotti, D., Huss, M.,
966 Dussaillant, I., Brun, F., and Kaab, A.: Accelerated global glacier mass loss in the early twenty-first
967 century, Nature, 592, 726-731, 10.1038/s41586-021-03436-z, 2021.
968 JAXA, J. A. E. A.: ALOS World 3D 30 meter DEM (V3.2), OpenTopography [dataset], 2021.
969 Kääb, A., Leinss, S., Gilbert, A., Bühler, Y., Gascoin, S., Evans, S. G., Bartelt, P., Berthier, E., Brun, F.,
970 Chao, W.-A., Farinotti, D., Gimbert, F., Guo, W., Huggel, C., Kargel, J. S., Leonard, G. J., Tian, L.,
971 Treichler, D., and Yao, T.: Massive collapse of two glaciers in western Tibet in 2016 after surge-like
972 instability, Nature Geoscience, 11, 114-120, 10.1038/s41561-017-0039-7, 2018.
973 Khosh Bin Ghomash, S., Caviedes-Voullieme, D., and Hinz, C.: Effects of erosion-induced changes to
974 topography on runoff dynamics, Journal of Hydrology, 573, 811-828, 10.1016/j.jhydrol.2019.04.018,
975 2019.
976 Lala, J. M., Rounce, D. R., and McKinney, D. C.: Modeling the glacial lake outburst flood process chain
977 in the Nepal Himalaya: reassessing Imja Tsho's hazard, Hydrology and Earth System Sciences, 22,
978 3721-3737, 10.5194/hess-22-3721-2018, 2018.
979 Linsbauer, A., Paul, F., Machguth, H., and Haeberli, W.: Comparing three different methods to model
980 scenarios of future glacier change in the Swiss Alps, Annals of Glaciology, 54, 241-253,
981 10.3189/2013AoG63A400, 2017.
982 Linsbauer, A., Frey, H., Haeberli, W., Machguth, H., Azam, M. F., and Allen, S.: Modelling glacier-bed
983 overdeepenings and possible future lakes for the glaciers in the Himalaya—Karakoram region, Annals
984 of Glaciology, 57, 119-130, 10.3189/2016AoG71A627, 2016.
985 Liu, K., Song, C., Ke, L., Jiang, L., Pan, Y., and Ma, R.: Global open-access DEM performances in Earth's
986 most rugged region High Mountain Asia: A multi-level assessment, Geomorphology, 338, 16-26,
987 10.1016/j.geomorph.2019.04.012, 2019.
988 Lützow, N., Veh, G., and Korup, O.: A global database of historic glacier lake outburst floods, Earth
989 Syst. Sci. Data Discuss., 2023, 1-27, 10.5194/essd-2022-449, 2023.
990 McClean, F., Dawson, R., and Kilsby, C.: Implications of Using Global Digital Elevation Models for
991 Flood Risk Analysis in Cities, Water Resources Research, 56, 10.1029/2020wr028241, 2020.
992 Mergili, M. and Pudasaini, S. P.: r.avaflow - The mass flow simulation tool. r.avaflow.direct Web
993 interface, 2024.
994 Mergili, M., Fischer, J.-T., Krenn, J., and Pudasaini, S. P.: r.avaflow v1, an advanced open-source
995 computational framework for the propagation and interaction of two-phase mass flows, Geoscientific
996 Model Development, 10, 553-569, 10.5194/gmd-10-553-2017, 2017.
997 Mergili, M., Jaboyedoff, M., Pullarello, J., and Pudasaini, S. P.: Back calculation of the 2017 Piz
998 Cengalo—Bondo landslide cascade with r.avaflow: what we can do and what we can learn, Natural
999 Hazards and Earth System Sciences, 20, 505-520, 10.5194/nhess-20-505-2020, 2020a.

Mergili, M., Frank, B., Fischer, J.-T., Huggel, C., and Pudasaini, S. P.: Computational experiments on the 1962 and 1970 landslide events at Huascarán (Peru) with r.avaflow: Lessons learned for predictive mass flow simulations, Geomorphology, 322, 15-28, 10.1016/j.geomorph.2018.08.032, 2018a.

Mergili, M., Pudasaini, S. P., Emmer, A., Fischer, J.-T., Cochachin, A., and Frey, H.: Reconstruction of the 1941 GLOF process chain at Lake Palcacocha (Cordillera Blanca, Peru), Hydrology and Earth System Sciences, 24, 93-114, 10.5194/hess-24-93-2020, 2020b.

Mergili, M., Emmer, A., Juricova, A., Cochachin, A., Fischer, J. T., Huggel, C., and Pudasaini, S. P.: How well can we simulate complex hydro-geomorphic process chains? The 2012 multi-lake outburst flood in the Santa Cruz Valley (Cordillera Blanca, Peru), Earth Surf Process Landf, 43, 1373-1389, 10.1002/esp.4318, 2018b.

Muthusamy, M., Casado, M. R., Butler, D., and Leinster, P.: Understanding the effects of Digital Elevation Model resolution in urban fluvial flood modelling, Journal of Hydrology, 596, 10.1016/j.jhydrol.2021.126088, 2021.

NASA-JPL: NASADEM Merged DEM Global 1 arc second V001. Distributed by OpenTopography, Distributed by OpenTopography [dataset], https://doi.org/10.5069/G93T9FD9, 2021.

NCHM: Reassessment of Potentially Dangerous Glacial Lakes in Bhutan, National Centre for Hydrology and Meteorology, Royal Government of Bhutan, National Center for Hydrology and Meteorology, Royal Government of Bhutan, PO Box: 2017, Thimphu, Bhutan, 54, 2019a.

NCHM: Detailed assessment report on GLOF hazard from Thorthormi glacial lakes and asssociated glaciers, Thimphu, 2019b.

NCHM: Action Taken Report Thorthormi Flood Incident 30th October 2023, National Center for Meteorology and Hydrology, Thimphu, 17, 2023.

Nie, Y., Liu, Q., Wang, J., Zhang, Y., Sheng, Y., and Liu, S.: An inventory of historical glacial lake outburst floods in the Himalayas based on remote sensing observations and geomorphological analysis, Geomorphology, 308, 91-106, 10.1016/j.geomorph.2018.02.002, 2018.

Nie, Y., Deng, Q., Pritchard, H. D., Carrivick, J. L., Ahmed, F., Huggel, C., Liu, L., Wang, W., Lesi, M., Wang, J., Zhang, H., Zhang, B., Lü, Q., and Zhang, Y.: Glacial lake outburst floods threaten Asia's infrastructure, Science Bulletin, 10.1016/j.scib.2023.05.035, 2023.

Obu, J., Westermann, S., Bartsch, A., Berdnikov, N., Christiansen, H. H., Dashtseren, A., Delaloye, R., Elberling, B., Etzelmüller, B., Kholodov, A., Khomutov, A., Kääb, A., Leibman, M. O., Lewkowicz, A. G., Panda, S. K., Romanovsky, V., Way, R. G., Westergaard-Nielsen, A., Wu, T., Yamkhin, J., and Zou, D.: Northern Hemisphere permafrost map based on TTOP modelling for 2000–2016 at 1 km2 scale, Earth-Science Reviews, 193, 299-316, 10.1016/j.earscirev.2019.04.023, 2019.

Pudasaini, S. P.: A general two-phase debris flow model, Journal of Geophysical Research: Earth Surface, 117, 10.1029/2011jf002186, 2012.

Pudasaini, S. P. and Krautblatter, M.: A two-phase mechanical model for rock-ice avalanches, Journal of Geophysical Research: Earth Surface, 119, 2272-2290, 10.1002/2014jf003183, 2014a.

Pudasaini, S. P. and Krautblatter, M.: A two-phase mechanical model for rock-ice avalanches, Journal of Geophysical Research: Earth Surface, 119, 2272-2290, 10.1002/2014jf003183, 2014b.

Pudasaini, S. P. and Mergili, M.: A Multi-Phase Mass Flow Model, Journal of Geophysical Research: Earth Surface, 124, 2920-2942, 10.1029/2019jf005204, 2019.

Rinzin, S., Zhang, G., and Wangchuk, S.: Glacial Lake Area Change and Potential Outburst Flood Hazard Assessment in the Bhutan Himalaya, Frontiers in Earth Science, 9, 10.3389/feart.2021.775195, 2021.

Rinzin, S., Zhang, G., Sattar, A., Wangchuk, S., Allen, S. K., Dunning, S., and Peng, M.: GLOF hazard, exposure, vulnerability, and risk assessment of potentially dangerous glacial lakes in the Bhutan Himalaya, Journal of Hydrology, 619, 10.1016/j.jhydrol.2023.129311, 2023.

Rounce, D., Watson, C., and McKinney, D.: Identification of Hazard and Risk for Glacial Lakes in the Nepal Himalaya Using Satellite Imagery from 2000–2015, Remote Sens-Basel, 9, 10.3390/rs9070654, 2017.

Rounce, D. R., McKinney, D. C., Lala, J. M., Byers, A. C., and Watson, C. S.: A new remote hazard and risk assessment framework for glacial lakes in the Nepal Himalaya, Hydrology and Earth System Sciences, 20, 3455-3475, 10.5194/hess-20-3455-2016, 2016.

Saksena, S. and Merwade, V.: Incorporating the effect of DEM resolution and accuracy for improved flood inundation mapping, Journal of Hydrology, 530, 180-194, 10.1016/j.jhydrol.2015.09.069, 2015.

Saltelli, A., Tarantola, S., Campolongo, F., and Ratto, M.: Sensitivity analysis in practice: a guide to assessing scientific models, Wiley Online Library2004.

Sattar, A., Haritashya, U. K., Kargel, J. S., Leonard, G. J., Shugar, D. H., and Chase, D. V.: Modeling lake outburst and downstream hazard assessment of the Lower Barun Glacial Lake, Nepal Himalaya, Journal of Hydrology, 598, 10.1016/j.jhydrol.2021.126208, 2021a.

Sattar, A., Goswami, A., Kulkarni, A. V., Emmer, A., Haritashya, U. K., Allen, S., Frey, H., and Huggel, C.: Future Glacial Lake Outburst Flood (GLOF) hazard of the South Lhonak Lake, Sikkim Himalaya, Geomorphology, 388, 10.1016/j.geomorph.2021.107783, 2021b.

Sattar, A., Allen, S., Mergili, M., Haeberli, W., Frey, H., Kulkarni, A. V., Haritashya, U. K., Huggel, C., Goswami, A., and Ramsankaran, R.: Modeling Potential Glacial Lake Outburst Flood Process Chains and Effects From Artificial Lake-Level Lowering at Gepang Gath Lake, Indian Himalaya, Journal of Geophysical Research: Earth Surface, 128, 10.1029/2022jf006826, 2023.

Sattar, A., Cook, K. L., Rai, S. K., Berthier, E., Allen, S., Rinzin, S., Van Wyk de Vries, M., Haeberli, W., Kushwaha, P., Shugar, D. H., Emmer, A., Haritashya, U. K., Frey, H., Rao, P., Gurudin, K. S. K., Rai, P., Rajak, R., Hossain, F., Huggel, C., Mergili, M., Azam, M. F., Gascoin, S., Carrivick, J. L., Bell, L. E., Ranjan, R. K., Rashid, I., Kulkarni, A. V., Petley, D., Schwanghart, W., Watson, C. S., Islam, N., Gupta, M. D., Lane, S. N., and Bhat, S. Y.: The Sikkim flood of October 2023: Drivers, causes and impacts of a multihazard cascade, Science, 0, eads2659, doi:10.1126/science.ads2659, 2025.

Schneider, D., Huggel, C., Cochachin, A., Guillén, S., and García, J.: Mapping hazards from glacier lake outburst floods based on modelling of process cascades at Lake 513, Carhuaz, Peru, Advances in Geosciences, 35, 145-155, 10.5194/adgeo-35-145-2014, 2014.

Schumann, G. J. P. and Bates, P. D.: The Need for a High-Accuracy, Open-Access Global DEM, Frontiers in Earth Science, 6, 10.3389/feart.2018.00225, 2018.

Shean, D.: High Mountain Asia 8-meter DEM mosaics derived from optical imagery, version 1, Boulder, CO: NASA National Snow and Ice Data Center Distributed Active Archive Center. doi, 10, 002214309790152555, 2017a.

Shean, D.: High Mountain Asia 8-meter DEM mosaics derived from optical imagery (1), NASA National Snow and Ice Data Center Distributed Active Archive Center [dataset], 2017b.

Shean, D. E., Alexandrov, O., Moratto, Z. M., Smith, B. E., Joughin, I. R., Porter, C., and Morin, P.: An automated, open-source pipeline for mass production of digital elevation models (DEMs) from very-high-resolution commercial stereo satellite imagery, ISPRS Journal of Photogrammetry and Remote Sensing, 116, 101-117, 10.1016/j.isprsjprs.2016.03.012, 2016.

Shrestha, F., Steiner, J. F., Shrestha, R., Dhungel, Y., Joshi, S. P., Inglis, S., Ashraf, A., Wali, S., Walizada, K. M., and Zhang, T.: HMAGLOFDB v1.0 – a comprehensive and version controlled database of glacier lake outburst floods in high mountain Asia, Earth Syst. Sci. Data Discuss., 2023, 1-28, 10.5194/essd-2022-395, 2023.

Shugar, D. H., Burr, A., Haritashya, U. K., Kargel, J. S., Watson, C. S., Kennedy, M. C., Bevington, A. R., Betts, R. A., Harrison, S., and Strattman, K.: Rapid worldwide growth of glacial lakes since 1990, Nature Climate Change, 10, 939-945, 10.1038/s41558-020-0855-4, 2020.

Shugar, D. H., Jacquemart, M., Shean, D., Bhushan, S., Upadhyay, K., Sattar, A., Schwanghart, W., McBride, S., de Vries, M. V. W., Mergili, M., Emmer, A., Deschamps-Berger, C., McDonnell, M., Bhambri, R., Allen, S., Berthier, E., Carrivick, J. L., Clague, J. J., Dokukin, M., Dunning, S. A., Frey, H., Gascoin, S., Haritashya, U. K., Huggel, C., Kääb, A., Kargel, J. S., Kavanaugh, J. L., Lacroix, P., Petley, D., Rupper, S., Azam, M. F., Cook, S. J., Dimri, A. P., Eriksson, M., Farinotti, D., Fiddes, J., Gnyawali, K. R., Harrison, S., Jha, M., Koppes, M., Kumar, A., Leinss, S., Majeed, U., Mal, S., Muhuri, A., Noetzli, J., Paul, F., Rashid, I., Sain, K., Steiner, J., Ugalde, F., Watson, C. S., and Westoby, M. J.: A massive rock

1101   and ice avalanche caused the 2021 disaster at Chamoli, Indian Himalaya, Science, 373, 300,
1102   10.1126/science.abh4455, 2021.

1103   Somos-Valenzuela, M. A., McKinney, D. C., Byers, A. C., Rounce, D. R., Portocarrero, C., and Lamsal,
1104   D.: Assessing downstream flood impacts due to a potential GLOF from Imja Tsho in Nepal, Hydrology
1105   and Earth System Sciences, 19, 1401-1412, 10.5194/hess-19-1401-2015, 2015.

1106   Taylor, C., Robinson, T. R., Dunning, S., Rachel Carr, J., and Westoby, M.: Glacial lake outburst floods
1107   threaten millions globally, Nature Communications, 14, 487, 10.1038/s41467-023-36033-x, 2023.

1108   Thompson, I., Shrestha, M., Chhetri, N., and Agusdinata, D. B.: An institutional analysis of glacial
1109   floods and disaster risk management in the Nepal Himalaya, International Journal of Disaster Risk
1110   Reduction, 47, 10.1016/j.ijdrr.2020.101567, 2020.

1111   Uuemaa, E., Ahi, S., Montibeller, B., Muru, M., and Kmoch, A.: Vertical Accuracy of Freely Available
1112   Global Digital Elevation Models (ASTER, AW3D30, MERIT, TanDEM-X, SRTM, and NASADEM), Remote
1113   Sens-Basel, 12, 10.3390/rs12213482, 2020.

1114   Vilca, O., Mergili, M., Emmer, A., Frey, H., and Huggel, C.: The 2020 glacial lake outburst flood process
1115   chain at Lake Salkantaycocha (Cordillera Vilcabamba, Peru), Landslides, 18, 2211-2223,
1116   10.1007/s10346-021-01670-0, 2021.

1117   Wang, W., Yang, X., and Yao, T.: Evaluation of ASTER GDEM and SRTM and their suitability in hydraulic
1118   modelling of a glacial lake outburst flood in southeast Tibet, Hydrological Processes, 26, 213-225,
1119   10.1002/hyp.8127, 2011.

1120   Wang, X., Guo, X., Yang, C., Liu, Q., Wei, J., Zhang, Y., Liu, S., Zhang, Y., Jiang, Z., and Tang, Z.: Glacial
1121   lake inventory of high-mountain Asia in 1990 and 2018 derived from Landsat images, Earth System
1122   Science Data, 12, 2169-2182, 10.5194/essd-12-2169-2020, 2020.

1123   Wang, Y., Hutter, K., and Pudasaini, S. P.: The Savage-Hutter theory: A system of partial differential
1124   equations for avalanche flows of snow, debris, and mud, ZAMM - Journal of Applied Mathematics
1125   and Mechanics / Zeitschrift für Angewandte Mathematik und Mechanik, 84, 507-527,
1126   10.1002/zamm.200310123, 2004.

1127   Watson, C. S., Carrivick, J., and Quincey, D.: An improved method to represent DEM uncertainty in
1128   glacial lake outburst flood propagation using stochastic simulations, Journal of Hydrology, 529, 1373-
1129   1389, 10.1016/j.jhydrol.2015.08.046, 2015.

1130   Westoby, M. J., Glasser, N. F., Brasington, J., Hambrey, M. J., Quincey, D. J., and Reynolds, J. M.:
1131   Modelling outburst floods from moraine-dammed glacial lakes, Earth-Science Reviews, 134, 137-159,
1132   10.1016/j.earscirev.2014.03.009, 2014.

1133   Westoby, M. J., Brasington, J., Glasser, N. F., Hambrey, M. J., Reynolds, J. M., Hassan, M. A. A. M., and
1134   Lowe, A.: Numerical modelling of glacial lake outburst floods using physically based dam-breach
1135   models, Earth Surface Dynamics, 3, 171-199, 10.5194/esurf-3-171-2015, 2015.

1136   Worni, R., Huggel, C., and Stoffel, M.: Glacial lakes in the Indian Himalayas--from an area-wide glacial
1137   lake inventory to on-site and modeling based risk assessment of critical glacial lakes, Sci Total
1138   Environ, 468-469 Suppl, S71-84, 10.1016/j.scitotenv.2012.11.043, 2013.

1139   Worni, R., Stoffel, M., Huggel, C., Volz, C., Casteller, A., and Luckman, B.: Analysis and dynamic
1140   modeling of a moraine failure and glacier lake outburst flood at Ventisquero Negro, Patagonian
1141   Andes (Argentina), Journal of Hydrology, 444-445, 134-145, 10.1016/j.jhydrol.2012.04.013, 2012.

1142   Zhang, G., Yao, T., Xie, H., Wang, W., and Yang, W.: An inventory of glacial lakes in the Third Pole
1143   region and their changes in response to global warming, Global and Planetary Change, 131, 148-157,
1144   10.1016/j.gloplacha.2015.05.013, 2015.

1145   Zhang, G., Bolch, T., Yao, T., Rounce, D. R., Chen, W., Veh, G., King, O., Allen, S. K., Wang, M., and
1146   Wang, W.: Underestimated mass loss from lake-terminating glaciers in the greater Himalaya, Nature
1147   Geoscience, 10.1038/s41561-023-01150-1, 2023a.

1148   Zhang, T., Wang, W., and An, B.: Heterogeneous changes in global glacial lakes under coupled climate
1149   warming and glacier thinning, Communications Earth & Environment, 5, 10.1038/s43247-024-01544-
1150   y, 2024.

1151 Zhang, T., Wang, W., An, B., and Wei, L.: Enhanced glacial lake activity threatens numerous
1152 communities and infrastructure in the Third Pole, Nature Communications, 14, 10.1038/s41467-023-
1153 44123-z, 2023b.
1154 Zheng, G., Mergili, M., Emmer, A., Allen, S., Bao, A., Guo, H., and Stoffel, M.: The 2020 glacial lake
1155 outburst flood at Jinwuco, Tibet: causes, impacts, and implications for hazard and risk assessment,
1156 The Cryosphere Discuss., 2021, 1-28, 10.5194/tc-2020-379, 2021a.
1157 Zheng, G., Allen, S. K., Bao, A., Ballesteros-Cánovas, J. A., Huss, M., Zhang, G., Li, J., Yuan, Y., Jiang, L.,
1158 Yu, T., Chen, W., and Stoffel, M.: Increasing risk of glacial lake outburst floods from future Third Pole
1159 deglaciation, Nature Climate Change, 11, 411-417, 10.1038/s41558-021-01028-3, 2021b.

1160